New acoustic velocity measurements on CaO-MgO-Al_2O_3-SiO_2 liquids: Reevaluation of the volume and compressibility of $CaMgSi_2O_6$-$CaAl_2Si_2O_8$ liquids to 25 GPa

Yuhui Ai[1] and Rebecca A. Lange[1]

Received 21 February 2007; revised 13 September 2007; accepted 7 December 2007; published 8 April 2008.

[1] Relaxed sound speed measurements on 12 liquids in the CaO-MgO-Al_2O_3-SiO_2 (CMAS) system have been performed from 1410 to 1620°C at 1 bar with a frequency sweep acoustic interferometer. In all liquids, the sound speeds either decrease or remain constant with increasing temperature. These data are combined with those in the literature to calibrate models for β_T and $(\partial V/\partial P)_T$ as a function of composition and temperature for CMAS liquids. CaO is the only oxide component that contributes to the temperature dependence of compressibility. The new compressibility models permit the bulk modulus ($K_{T,0}$) of $CaMgSi_2O_6$ (Di), $CaAl_2Si_2O_8$ (An), and the Di_{64}-An_{36} eutectic liquid to be directly obtained. These results are used to uniquely constrain values for the pressure dependence of the bulk modulus ($K_0' = dK_0/dP$) in a third-order Birch-Murnaghan equation of state (EOS) for these three liquids from shock wave data in the literature. The revised K_0' value is 6.8 (versus 6.9) for $CaMgSi_2O_6$ liquid, 4.7 (versus 5.3) for $CaAl_2Si_2O_8$ liquid, and 5.6 (versus 4.85) for Di_{64}-An_{36} liquid. Information on both $K_{T,0}$ and K_0' allows the density and compressibility for each of these three liquids to be calculated as a function of pressure to 25 GPa. Both the molar volume and isothermal compressibility of $CaMgSi_2O_6$-$CaAl_2Si_2O_8$ liquids mix ideally between 0 and 25 GPa. The dominant mechanism of compression at low pressure (0–5 GPa) for all three liquids ($CaMgSi_2O_6$, $CaAl_2Si_2O_8$, and the Di_{64}-An_{36} eutectic) is topological, whereas gradual Al/Si coordination change plays an increasingly important role at higher pressure as topological mechanisms of compression are diminished.

Citation: Ai, Y., and R. Lange (2008), New acoustic velocity measurements on CaO-MgO-Al_2O_3-SiO_2 liquids: Reevaluation of the volume and compressibility of $CaMgSi_2O_6$-$CaAl_2Si_2O_8$ liquids to 25 GPa, *J. Geophys. Res.*, *113*, B04203, doi:10.1029/2007JB005010.

1. Introduction

[2] Partial melting processes in the deep Earth, and the magmatism that results, are an important mechanism for transferring mass and energy from the Earth's interior to the surface. In order to develop thermodynamic models of partial melting of the mantle [e.g., *Ghiorso et al.*, 2002] and to characterize the subsequent melt transport, it is necessary to obtain a comprehensive equation of state (P-V-T relation) for magmatic liquids. Although the systematics of melt density are fairly well established at 1 bar, the compressional properties are less well known. Despite the pioneering efforts of *Rivers and Carmichael* [1987], *Kress et al.* [1988], *Kress and Carmichael* [1991], *Secco et al.* [1991], *Webb and Courtial* [1996] and others, there is still a significant need to expand 1-bar sound speed measurements on silicate liquids over a wide range of composition and temperature.

[3] In this study we focus on the CaO-MgO-Al_2O_3-SiO_2 (CMAS) quaternary, which includes the diopside component, $CaMgSi_2O_6$ (Di), the anorthite component, $CaAl_2Si_2O_8$ (An), as well as the eutectic Di_{64}-An_{36}, which is often used as a model basalt composition. This work complements previous sound speed measurements on various liquids in the CaO-Al_2O_3-SiO_2 ternary [*Webb and Courtial*, 1996], and liquids along the Di-An join [*Rivers and Carmichael*, 1987; *Secco et al.*, 1991]. By expanding the average temperature interval over which sound speeds are measured for each sample, a more robust evaluation of the temperature dependence to melt compressibility can be made. This study also reports the first sound speed measurements on MgO-Al_2O_3-SiO_2 liquids.

[4] One of the most important applications of this study is to reevaluate the equation of state for the following three liquids, $CaMgSi_2O_6$, $CaAl_2Si_2O_8$, and the Di_{64}-An_{36} eutectic, for which high-pressure density data are available from shock wave experiments [*Rigden et al.*, 1988, 1989]. With independent determinations of the bulk modulus ($K_{T,0}$) for each liquid from sound speed data, unique constraints on $K_0'(= dK_0/dP)$ can be made for each liquid (in a third-order Birch-Murnaghan EOS), which is required to evaluate any

[1]Department of Geological Sciences, University of Michigan, Ann Arbor, Michigan, USA.

0148-0227/08/2007JB005010$09.00

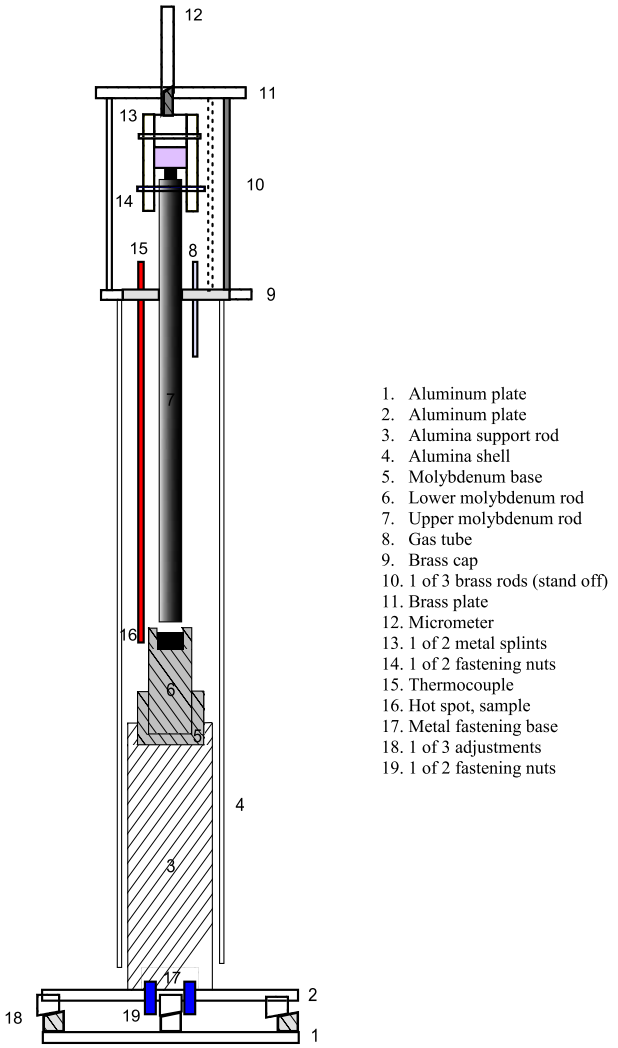

Figure 1. A schematic illustration of the frequency sweep acoustic interferometer.

compositional dependence to K_0' values and whether the volumetric properties of $CaMgSi_2O_6$-$CaAl_2Si_2O_8$ liquids mix ideally at high pressure.

[5] A final application in this study is a scrutiny of how the compressibility (β_T) of $CaMgSi_2O_6$ liquid varies with pressure relative to that for crystalline diopside, and similarly how the compressibility of $CaAl_2Si_2O_8$ liquid varies with pressure relative to that for crystalline anorthite. This exercise reveals the dominance of topological mechanisms of compression (involving dynamic bond breaking) in these two liquids at low pressure (0–5 GPa), distinct from Al/Si coordination change or mechanisms of compression available to minerals (changes in bond angles and bond lengths).

2. Experimental Method and Liquids

2.1. Experimental Apparatus and Method

[6] The frequency sweep ultrasonic interferometer (Figure 1) described by *Ai and Lange* [2004b] was employed for the sound speed measurements. In this apparatus, the transducer functions as both the transmitter and receiver. It is mounted on the top of a molybdenum buffer rod (40 cm long by 1.9 cm diameter), the opposite end of which is well polished and immersed in the liquid, which is held in a crucible with a well-polished inner base. The crucible is a 2 cm deep by 2.4 cm diameter hollow drilled into a molybdenum lower buffer rod that is 2.8 cm in diameter and 10 cm long. The interferometer is inserted in a vertical alumina tube inside a Deltech furnace, through which a reducing gas mixture (99% Ar/1% CO) flows to prevent oxidation of the molybdenum buffer rod and crucible. In addition to the transducer, a water-cooling jacket and a micrometer are mounted on top of the upper buffer rod by a brass fixture. The micrometer is used to precisely adjust and record (with resolution 0.001 mm) the position of the upper rod. The lower rod (crucible) is supported by an alumina rod, which extends to the outside of the furnace and is attached to an aluminum plate with three height adjustment screws. These permit adjustment of the lower buffer rod to ensure that the surface of the crucible bottom is parallel to the end surface of the upper buffer rod (Figure 1).

[7] In an experiment, an acoustic pulse is first programmed and formed in a computer and then its format (amplitude, frequency, duration) is delivered to an arbitrary wave generator that generates the pulse and drives the gated amplifier to produce a power output to the transducer. The transducer converts the electronic energy to an acoustic pulse that travels down the molybdenum upper buffer rod. When the acoustic signal reaches the rod-melt interface, part is propagated into the liquid and part is reflected back up the upper buffer rod. The part that is transmitted through the liquid reflects off the polished bottom of the crucible and these mirror reflections return up the buffer rod and are received by the transducer. The return signals, which are well described by the theoretical acoustic model of *Ai and Lange* [2004a], are delivered to a preamplifier for amplification and then to the data acquisition system for signal processing, where a Fourier transform on the return echo is performed to analyze the frequency response.

[8] The frequency sweep method employed in this study differs from the variable-path length method used in previous studies of silicate melt sound speeds [e.g., *Katahara et al.*, 1981; *Rivers and Carmichael*, 1987; *Kress et al.*, 1988; *Webb and Courtial*, 1996] in two critical respects. First, the initial acoustic pulse that is sent down the upper buffer rod is short ($\sim$1 μs) compared to the pulse durations used in previous studies ($\sim$25 μs [*Rivers and Carmichael*, 1987]). By significantly shortening the pulse duration it is possible to receive two mirror reflections off the bottom of the crucible before interfering pulses (discussed by *Ai and Lange* [2004a, 2004b]) are returned up the buffer rod. Second, the initial pulse does not consist of a single frequency but instead is a wideband pulse that encompasses a wide range of frequencies that span $\sim$2 MHz, with centered frequencies at 4.5 and 6.0 MHz. This allows maxima/minima in the returned signal to be evaluated as a periodic function of frequency, Δf, from which the liquid sound speed (c) is measured from the relation: $\Delta f = c/2S$. If both Δf and S (melt thickness) are known, then c is readily calculated.

[9] In practice, a more accurate and precise measurement is made of the difference in melt thickness ($\Delta S = S_1 - S_2$) between two rod positions rather than the absolute values of

Table 1. Composition of 12 CMAS Samples[a]

Sample	SiO_2	Al_2O_3	MgO	CaO
RC-14	50.20	24.60	—	25.20
LC-4	36.70	27.09	—	36.21
LC-8	60.74	9.46	—	29.80
LC-9	61.20	9.51	28.64	0.66
LC-10	56.11	10.48	33.27	0.14
LC-11	49.02	13.07	37.82	0.09
LC-12	51.14	17.28	14.12	17.48
LC-13	46.74	15.27	15.90	22.09
SN-4	46.65	10.25	11.80	31.30
SN-13	55.76	—	27.85	16.40
LC-14	49.83	—	24.55	25.63
LC-15	47.59	—	17.12	35.29

[a]In mol %. Wet chemical analyses from *Lange and Carmichael* [1987] for LC samples, from *Nelson and Carmichael* [1979] for SN samples, and from *Rivers and Carmichael* [1987] for RC samples.

melt thickness (S_1 and S_2) at these two rod positions. Because liquid sound speed is independent of melt thickness, a frequency sweep experiment performed for two different liquid depths (S_1 and S_2) lead to two different Δf values (Δf_1 and Δf_2). In combination, the following relationship holds:

$$c = \left| \frac{2\Delta S}{\Delta f_2^{-1} - \Delta f_1^{-1}} \right|. \quad (1)$$

Therefore, for the experiments performed in this study, measurements were made at several rod positions for each centered frequency at a given temperature.

2.2. Experimental Liquids

[10] The wet chemically analyzed compositions of the samples are listed in Table 1. All 12 samples were previously synthesized and analyzed by *Lange and Carmichael* [1987] (LC-4, LC-8, LC-9, LC-10, LC-11, LC-12, LC-13, LC-14, LC-15), *Nelson and Carmichael* [1979] (SN-4, SN-13), and *Rivers and Carmichael* [1987] (RC-14). Among these 12 samples, three are in the CaO-MgO-SiO_2 (CMS) ternary (including $CaMgSi_2O_6$; LC-14), three are in the CaO-Al_2O_3-SiO_2 (CAS) ternary (including $CaAl_2Si_2O_8$; RC-14), three are in the MgO-Al_2O_3-SiO_2 (MAS) ternary, and three are in the CMAS quaternary. Approximately five grams of each sample was loaded into the crucible prior to each experiment, which is sufficient to produce a melt thickness of >3 mm during the high-temperature experiments. This allowed melt thicknesses of 2–3 mm for different rod positions. The heating and cooling process for each sample took 3–4 h, but the sample was at high temperature for less than 3 h in most cases.

3. Experimental Results

[11] The sound speed data on the 12 liquids are presented in Table 2 for each frequency and temperature of measurement. Experimental errors are $\leq$40 m s^{-1} on the basis of reproducibility, when a sample is reloaded and measured weeks or months apart. In contrast, the reproducibility for measurements replicated in a single afternoon, without reloading the sample, is $\leq$10 m s^{-1}. This difference may relate to errors in estimates of melt thickness and, to a smaller degree, temperature. Therefore, error is introduced each time a sample is reloaded and an experiment is set up from scratch; thus a maximum error of $\leq$ 40 m s^{-1} is reported for all measurements. Sound speed measurements were conducted at centered frequencies of 6.0 MHz, and either 4.5 MHz or 4.8 MHz. Temperatures of measurement ranged from highs of 1607–1622°C and were extended as low as possible (1410–1564°C) until significant attenuation or pulse dispersion was observed in the liquid, at which point the liquid is unrelaxed (the deformation of the echo shape is visible because of the broadband spectrum of the short $\sim$1 μs pulse). The density (ρ) and adiabatic compressibility (β_S) of each liquid at each temperature of measurement are also listed in Table 2. The densities are known from the measurements of *Lange and Carmichael* [1987] and *Lange* [1997], which allow the adiabatic compressibility of each sample to be calculated from the relation: $\beta_S = 1/\rho c^2$.

3.1. Modeling Sound Speed

[12] Although sound speed is not an extensive thermodynamic property, it is nonetheless convenient to model its variation with composition and temperature using the following linear model:

$$c^{liq}(X,T) = \sum X_i \left(c_{i,1673} + \frac{\partial c_i}{\partial T}(T - 1673K) \right) \quad (2)$$

where X_i is the mole fraction of each oxide component, c_i is the "partial molar" sound speed for each oxide component at a reference temperature (1673 K), and $\partial c_1/\partial T$ is its temperature dependence. The linear model in equation (2) was also used by *Ghiorso and Kress* [2004] and permits a comparison of our fitted results with theirs (Tables 3a and 3b).

[13] The data from Table 2 were used in a regression of equation (2), along with additional sound speed measurements on CMAS liquids from the literature. These include data from *Rivers and Carmichael* [1987]: $CaMgSi_2O_6$ (Di; RC-13), $CaAl_2Si_2O_8$ (An; RC-14), $CaSiO_3$ (RC-10), and Di_{50}-An_{50} (RC-15), as well as data on the Di_{64}-An_{36} eutectic from *Secco et al.* [1991]. Additionally, *Webb and Courtial* [1996] report sound speed data for five CAS liquids, two of which contain $\leq$11 mol % SiO_2. These two silica-poor, CaO-Al_2O_3 liquids (Ca09.23 and Ca11.39) were not included in our regression because these are structurally and compositionally distinct from magmatic liquids. Data for two liquids (Ca53.12 and Ca38.27) from *Webb and Courtial* [1996] were included in the regression reported in Table 3b, although a fifth sample (Ca36.16) was not included, because it was a major outlier (>60 m s^{-1}), outside experimental error, in contrast to all other 19 samples. Note that this does not imply that the sound speed measurements on this sample are inaccurate, and the compressibility of this liquid composition is discussed below (in the section with the header: Recommended models).

[14] The results of the regression to equation (2) are presented in Table 3a, where fitted values for c_i and $\partial c_i/\partial T$ are shown. The overall quality of the fit is excellent, with an adjusted R^2 = 0.9932 and an average error of ± 0.57%. For comparison, the results of the *Ghiorso and Kress* [2004] sound speed regression are given in Table 3b. Both models show that values for c_i increase in the order $SiO_2 < Al_2O_3 <$ MgO < CaO, although the results from this study indicate that the only oxide component that contributes to the

Table 2. Sound Speed, Density, and Adiabatic Compressibility Data for CMAS Liquids

Sample	T(°C)	f(MHz)	c(m s^{-1})	ρ(g cm^{-3})	β_S(10^{-2} GPa^{-1})	β_T(10^{-2} GPa^{-1})	dV/dP(10^{-4} cm^3 bar^{-1})
RC-14	1564	4.8	2804	2.569	4.950	4.994	−1.346
RC-14	1564	6.0	2802	2.569	4.961	5.004	−1.349
RC-14	1581	4.8	2802	2.568	4.960	5.004	−1.350
RC-14	1581	6.0	2799	2.568	4.971	5.015	−1.353
RC-14	1607	4.8	2794	2.566	4.993	5.038	−1.360
RC-14	1607	6.0	2802	2.566	4.965	5.009	−1.352
LC-4	1507	4.8	2997	2.679	4.156	4.244	−1.109
LC-4	1507	6.0	2990	2.679	4.176	4.263	−1.114
LC-4	1560	4.8	2988	2.671	4.193	4.283	−1.122
LC-4	1560	6.0	2980	2.671	4.215	4.305	−1.128
LC-4	1611	4.8	2979	2.664	4.229	4.322	−1.135
LC-4	1611	6.0	2978	2.664	4.232	4.324	−1.136
LC-8	1536	4.5	2788	2.521	5.103	5.177	−1.291
LC-8	1536	6.0	2794	2.521	5.081	5.155	−1.285
LC-8	1571	4.5	2770	2.517	5.178	5.253	−1.312
LC-8	1571	6.0	2765	2.517	5.196	5.272	−1.316
LC-8	1610	6.0	2780	2.513	5.149	5.226	−1.307
LC-9	1517	4.8	2673	2.477	5.650	5.746	−1.354
LC-9	1569	4.8	2658	2.472	5.726	5.825	−1.376
LC-9	1569	6.0	2655	2.472	5.739	5.838	−1.379
LC-9	1620	4.8	2676	2.467	5.657	5.758	−1.363
LC-9	1620	6.0	2665	2.467	5.708	5.809	−1.375
LC-10	1454	4.8	2691	2.521	5.479	5.585	−1.283
LC-10	1454	6.0	2695	2.521	5.462	5.601	−1.286
LC-10	1515	4.8	2729	2.513	5.342	5.469	−1.260
LC-10	1515	6.0	2731	2.513	5.335	5.461	−1.258
LC-10	1600	4.8	2712	2.503	5.431	5.564	−1.287
LC-10	1600	6.0	2712	2.503	5.431	5.564	−1.287
LC-11	1473	4.8	2775	2.571	5.050	5.208	−1.176
LC-11	1473	6.0	2770	2.571	5.069	5.226	−1.180
LC-11	1516	4.8	2781	2.565	5.040	5.202	−1.178
LC-11	1516	6.0	2788	2.565	5.015	5.176	−1.172
LC-11	1569	4.8	2769	2.558	5.099	5.265	−1.195
LC-11	1569	6.0	2768	2.558	5.103	5.268	−1.196
LC-11	1622	4.8	2779	2.550	5.077	5.247	−1.195
LC-11	1622	6.0	2780	2.550	5.073	5.243	−1.194
LC-12	1463	4.8	2803	2.573	4.947	5.031	−1.248
LC-12	1463	6.0	2806	2.573	4.937	5.021	−1.245
LC-12	1548	4.8	2819	2.563	4.910	4.998	−1.245
LC-12	1548	6.0	2816	2.563	4.920	5.008	−1.247
LC-12	1620	4.8	2820	2.555	4.922	5.013	−1.252
LC-12	1620	6.0	2820	2.555	4.922	5.013	−1.252
LC-13	1485	4.5	2914	2.614	4.506	4.634	−1.107
LC-13	1485	6.0	2908	2.614	4.524	4.653	−1.112
LC-13	1514	4.5	2905	2.609	4.541	4.671	−1.118
LC-13	1514	6.0	2902	2.609	4.550	4.681	−1.120
LC-13	1570	4.5	2906	2.601	4.552	4.686	−1.125
LC-13	1570	6.0	2908	2.601	4.546	4.680	−1.123
LC-13	1614	4.5	2890	2.595	4.614	4.751	−1.143
LC-13	1614	6.0	2871	2.595	4.675	4.812	−1.158
SN-4	1544	4.8	3055	2.627	4.079	4.256	−0.985
SN-4	1608	4.8	3015	2.616	4.206	4.388	−1.020
SN-13	1463	4.8	2874	2.563	4.724	4.960	−1.044
SN-13	1463	6.0	2870	2.563	4.737	4.973	−1.046
SN-13	1548	4.8	2875	2.547	4.749	4.996	−1.058
SN-13	1548	6.0	2871	2.547	4.763	5.009	−1.060
SN-13	1620	4.8	2853	2.534	4.848	5.103	−1.086
SN-13	1620	6.0	2856	2.534	4.838	5.092	−1.084
LC-14	1426	4.5	3051	2.640	4.070	4.405	−0.905
LC-14	1426	6.0	3035	2.640	4.113	4.362	−0.896
LC-14	1530	4.5	3012	2.616	4.213	4.512	−0.935
LC-14	1530	6.0	3015	2.616	4.205	4.521	−0.937
LC-14	1614	4.5	2989	2.598	4.309	4.594	−0.959
LC-14	1614	6.0	3001	2.598	4.274	4.628	−0.966
LC-15	1410	4.8	3185	2.679	3.679	3.981	−0.824
LC-15	1410	6.0	3183	2.679	3.684	3.985	−0.825
LC-15	1464	4.8	3175	2.666	3.721	4.030	−0.838
LC-15	1464	6.0	3175	2.666	3.723	4.033	−0.838
LC-15	1516	4.8	3163	2.654	3.767	4.084	−0.866
LC-15	1516	6.0	3161	2.654	3.772	4.089	−0.867
LC-15	1570	4.8	3151	2.641	3.814	4.139	−0.882

Table 2. (continued)

Sample	T(°C)	f(MHz)	c(m s^{-1})	ρ(g cm^{-3})	β_S(10^{-2} GPa^{-1})	β_T(10^{-2} GPa^{-1})	dV/dP(10^{-4} cm^3 bar^{-1})
LC-15	1570	6.0	3146	2.641	3.826	4.152	−0.885
LC-15	1620	4.8	3136	2.629	3.868	4.201	−0.899
LC-15	1620	6.0	3140	2.629	3.858	4.191	−0.897

temperature dependence of the sound speed data is CaO. Moreover, the fitted value for $\partial c_{CaO}/\partial T$ is negative, so that the sound speeds of CMAS liquids are expected to either remain constant or decrease with increasing temperature. In contrast, the sound speed model of *Ghiorso and Kress* [2004] (Table 3b) has fitted values for $\partial c_{SiO_2}/\partial T$, $\partial c_{Al_2O_3}/\partial T$ and $\partial c_{MgO}/\partial T$ that are positive and of higher magnitude than the negative value for $\partial c_{CaO}/\partial T$. Their model, however, is based on a regression on a wide compositional range of liquids that extends beyond the CMAS system.

[15] In Figure 2a–2l, the sound speed measurements for the 12 liquids obtained in this study are compared to the predicted values based on the results from this study (Table 3a) versus that presented by *Ghiorso and Kress* [2004] (Table 3b). The most important contrast between the two models is the negative (or zero) versus positive temperature dependence of the predicted sound speeds. *Ghiorso and Kress* [2004] did not have access to the expanded data set for CMAS liquids presented in Table 2, and so it is not surprising that their model cannot recover the measured sound speeds for many of these liquids within the maximum experimental error ($\leq$40 m s^{-1}). However, even for liquids from the literature used in the calibration of the *Ghiorso and Kress* [2004] model, the measured negative temperature dependence of the sound speeds is not recovered (e.g., Ca53.12 and Ca38.27 of *Webb and Courtial* [1996]) (see Figures 3a and 3b). The most striking example is seen with the data of *Secco et al.* [1991] for the Di_{64}-An_{36} eutectic that span ~300° and clearly show that sound speed decreases with temperature for this liquid (Figure 3c). The negative temperature dependence is well recovered by the results from this study (Table 3a), in contrast to the strong positive temperature dependence predicted by *Ghiorso and Kress* [2004] (Table 3b).

[16] The fitted parameters in Table 3a should only be applied to the calculation of liquid sound speeds over the temperature interval 1300–1650°C, and for liquids with 35–60 mol % SiO_2, $\leq$30 mol % Al_2O_3, $\leq$40 mol % MgO, and $\leq$50 mol % CaO. In other words, the model should only be used for interpolation within the temperature and compositional range of the data set used for its calibration. Caution should be applied when extrapolations are performed because the linear model in equation (2) is strictly empirical and has no theoretical foundation. Therefore, when extrapolations in composition and temperature are required, it is preferable to model the isothermal compressibility (β_T) or $(\partial V/\partial P)_T$ of the CMAS liquids.

3.2. Modeling Isothermal Compressibility

[17] The sound speed and density data compiled in Table 2 were used to calculate the adiabatic compressibility from the relation: $\beta_s = 1/\rho c^2$. This calculation was also applied to sound speed data on CMAS liquids from the literature [*Rivers and Carmichael*, 1987; *Secco et al.*, 1991; *Webb and Courtial*, 1996], described in the previous section. For an average error in sound speed of ~1.0% and an error in density of ~0.3%, the propagated uncertainty in β_S is ~1.6%. The adiabatic compressibility (β_S) is converted to isothermal compressibility (β_T) from the relation:

$$\beta_T = \beta_S + \frac{TV_T\alpha^2}{Cp}, \tag{3}$$

where T is temperature in degrees kelvin, V_T is the molar volume at temperature T, α is the thermal expansion coefficient, and C_p is molar heat capacity. The model of *Lange* [1997] was used to calculate V_T and α for the CMAS liquids, whereas the model of *Lange and Navtrotsky* [1992] was used to calculate the C_p of these melts. The difference between β_T and β_T ranges from ~1 to 8% of the value for β_S for the CMAS liquids. The propagated uncertainty in the final value for β_T is ~1.8%.

[18] *Rivers and Carmichael* [1987] derived a theoretically valid equation that describes the dependence of β_T on composition for an ideal solution. In this model, β_T varies as a linear function of the volume fraction of each oxide component:

$$\beta_T(X) = \sum X_i \frac{\overline{V}_{i,T}}{V_T}\overline{\beta}_{i,T} \tag{4}$$

where X_i is the mole fraction of each oxide component i, $\overline{V}_{i,T}$ is the partial molar volume of each oxide component i at temperature T, $V_{\underline{T}}$ is the molar volume of the liquid at temperature T, and $\overline{\beta}_i$ is the compressibility coefficient for each oxide component i.

Table 3a. Regression results for Equation (4) Using Sound Speed Data in Table 2 and From the Literature[a]

Oxide Component	C_i (1673K)± 1σ(m s^{-1})	$\partial c_i / \partial T$ ± 1σ(m (s K)$^{-1}$)
SiO_2	2178 ± 16	-
Al_2O_3	2650 ± 20	-
MgO	3600 ± 24	-
CaO	4241 ± 21	−0.51 ± 0.08

[a]Total of 153 observations; R^2 = 0.9999, adjusted R^2 = 0.9932, and average error is 0.57%.

Table 3b. Regression Results From *Ghiorso and Kress* [2004, Table 9][a]

Oxide Component	C_i (1673K)(m s^{-1})	$\partial c_i / \partial T$ (m (s K)$^{-1}$)
SiO_2	2322	0.40
Al_2O_3	2732	0.50
MgO	3350	0.27
CaO	3967	−0.21

[a]Only the SiO_2, Al_2O_3, MgO and CaO components are shown for comparison to this study. Fitted errors are not reported.

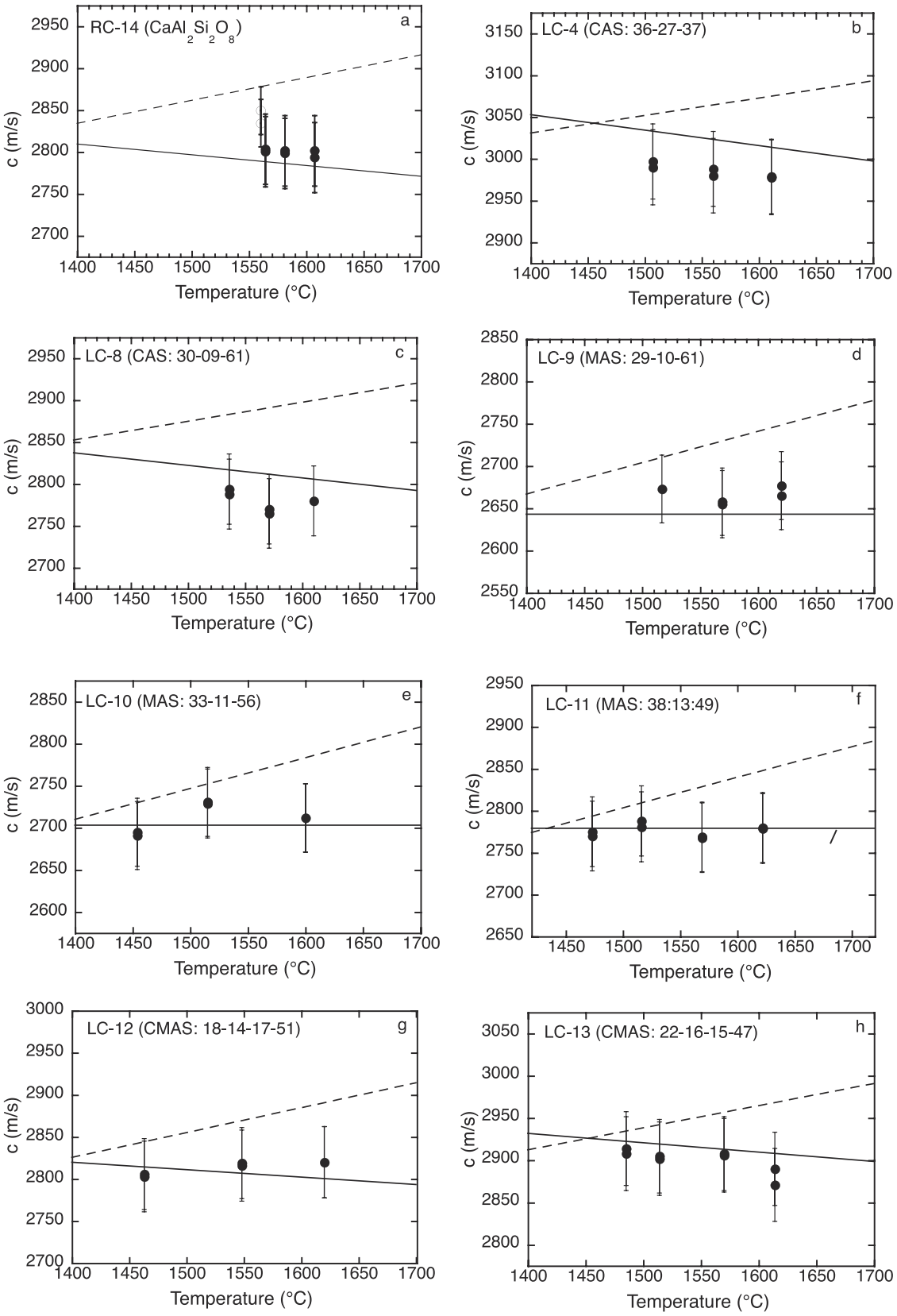

Figure 2. Plots of sound speed versus temperature for samples (a) RC-14, (b) LC-4, (c) LC-8, (d) LC-9, (e) LC-10, (f) LC-11, (g) LC-12, (h) LC-13, (i) SN-4, (j) SN-13, (k) LC-14, and (l) LC-15, respectively. The solid dots are from this study, whereas the open circles for LC-14 are from *Rivers and Carmichael* [1987]. The solid line is the calculated sound speed from the model parameters in Table 3a, whereas the dashed line is the calculated sound speed from the model of *Ghiorso and Kress* [2004].

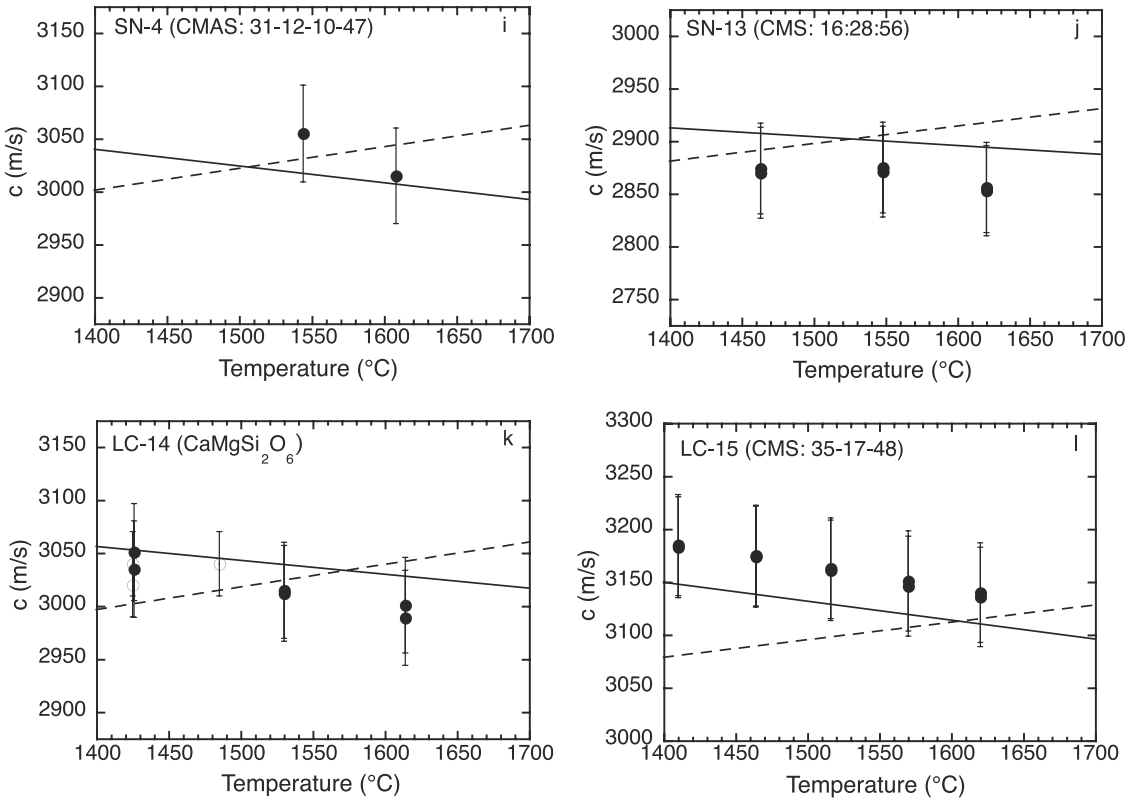

Figure 2. (continued)

[19] Here the model is expanded to include a linear dependence on temperature:

$$\beta_T(X) = \sum X_i \frac{\overline{V}_{i,T}}{V_T}\left(\overline{\beta}_{i,1673} + \frac{\partial \overline{\beta}_i}{\partial T}(T - 1673K)\right). \quad (5)$$

The data from both this study (Table 2) and from the literature [*Rivers and Carmichael*, 1987; *Secco et al.*, 1991; *Webb and Courtial*, 1996] were used in a regression of equation (5) and the results of the fit are presented in Table 4. The overall quality of the fit is excellent, with a R^2 = 0.9998 and an average error of ± 1.05%. Once again, the only component that contributes to the temperature dependence of compressibility is CaO. The results indicate that values for $\overline{\beta}_i$ decrease in the order $SiO_2 > Al_2O_3 > MgO > CaO$. SiO_2 and Al_2O_3 are the most compressible components, whereas MgO and CaO are highly incompressible (Table 4). In fact, the fitted value for $\overline{\beta}_{CaO}$ is negative, which clearly cannot be applied to pure CaO liquid. The third column in Table 4 is simply the inverse of the fitted $\overline{\beta}_i$ terms, which expresses the compressibility of each oxide component in terms of the bulk modulus.

3.3. Modeling $(\partial V/\partial P)_T$

[20] A final regression equation is presented for $(\partial V/\partial P)_T$, the derivative of molar volume with pressure, which is defined as $(\partial V/\partial P)_T = -V_T\ \beta_T$. For an ideal solution, $(\partial V/\partial P)_T$ varies as a linear function of composition:

$$\left(\frac{\partial V}{\partial P}\right)_T(X) = \sum X_i \left(\frac{\partial \overline{V}_i}{\partial P}\right)_T. \quad (6)$$

Following *Rivers and Carmichael* [1987] and *Kress and Carmichael* [1991], the model is expanded to include a linear dependence on temperature:

$$\left(\frac{\partial V}{\partial P}\right)_T(X,T) = \sum X_i \left(\frac{\partial \overline{V}_{i,1673}}{\partial P} + \frac{\partial^2 \overline{V}_i}{\partial P \partial T}(T - 1673K)\right). \quad (7)$$

The results of the regression to equation (7) are shown in Table 5a, and the overall quality of the fit is excellent, with a R^2 = 0.9998 and an average error of ±1.05%. The fitted values of $\partial \overline{V}_i/\partial P)_T$ indicate that SiO_2 and Al_2O_3 are the most compressible components (-1.922 and -1.692×10^{-4} cm^3 bar^{-1}, respectively), whereas the fitted values of $(\partial \overline{V}_i/\partial P)_T$ for MgO and CaO are both close to zero (-0.073 and 0.330×10^{-4} cm^3 bar^{-1}, respectively). The positive value for $(\partial \overline{V}_{CaO}/\partial P)_T$ indicates that it cannot be applied to pure CaO liquid. Again, the only compositional component that contributes to the temperature dependence of $(\partial V/\partial P)_T$ within statistical significance is CaO. For convenience, values of $\overline{V}_i$ for each oxide component from *Lange* [1997] are listed in Table 5a. Together with fitted values of $(\partial \overline{V}_i/\partial P)_T$, the bulk modulus for each component (K_i) can be calculated from the relation: $K_i = \overline{V}_i(\partial \overline{V}_i/\partial P)$. These values for K_i are listed in Table 5a and are nearly identical to those in given in Table 4, which illustrates the equivalence of the β_T and $(\partial V/\partial P)_T$ models.

[21] The fitted terms for $(\partial \overline{V}_i/\partial P)_T$ listed in Table 5a are similar to those presented by *Kress and Carmichael* [1991] (shown in Table 5b), which are derived from a regression on a wider compositional range of liquids that extends beyond the CMAS system. The fitted errors on $(\partial \overline{V}_i/\partial P)_T$ are nearly an order of magnitude smaller for Al_2O_3, MgO,

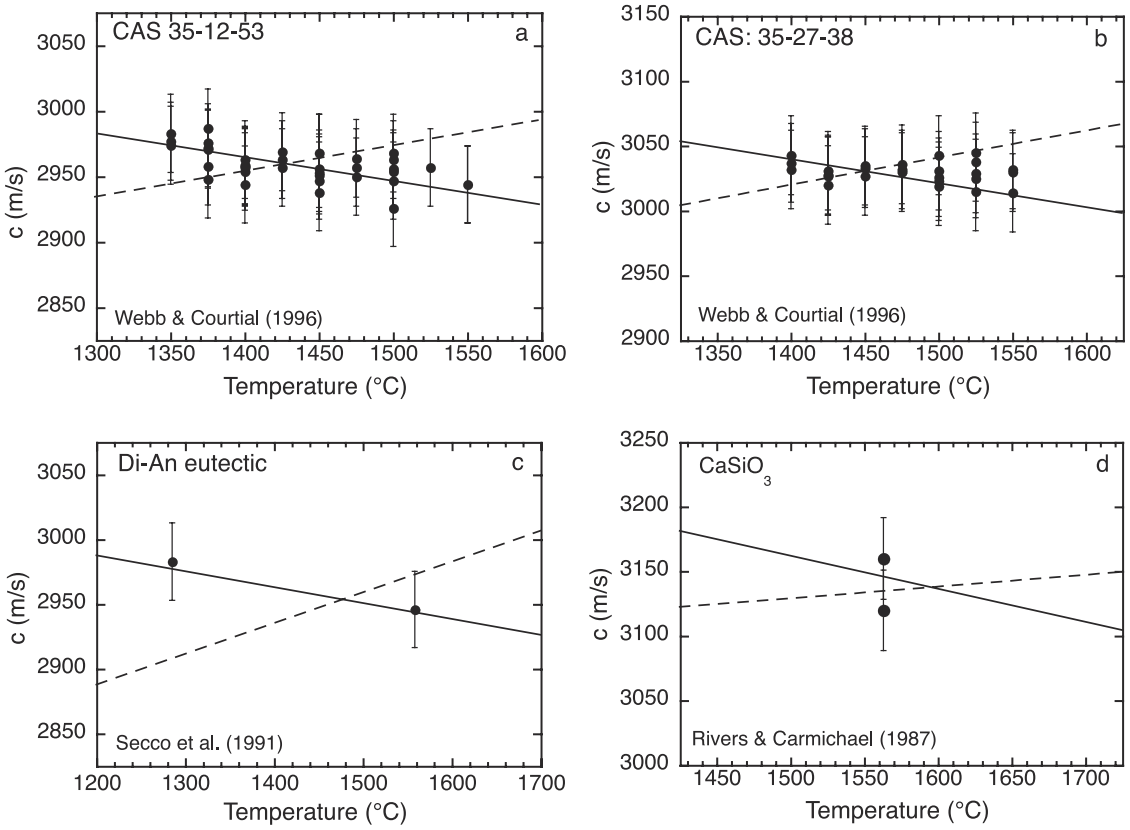

Figure 3. Plots of sound speed versus temperature for four sample liquids from the literature, including (a) CAS 35-12-53 and (b) CAS 35-27-38 from *Webb and Courtial* [1996], the (c) Di_{64}-An_{36} eutectic from *Secco et al.* [1991], and (d) $CaSiO_3$ from *Rivers and Carmichael* [1987]. The solid line is the calculated sound speed from the model parameters in Table 3a, whereas the dashed line is the calculated sound speed from the model of *Ghiorso and Kress* [2004].

and CaO in Table 5a (this study) than in Table 5b [*Kress and Carmichael*, 1991], which reflects the benefit of the new experimental data presented in this study in Table 2.

3.4. Recommended Models

[22] Of the three models presented above, only those for β_T and $(\partial V/\partial P)_T$ are theoretically valid for ideal solutions (equations (5) and (7), respectively), whereas the linear model for sound speed (equation (2)) is strictly empirical. The problem with the empirical sound speed model is best illustrated by examining sample Ca36.16 (36, 16, and 48 mol % SiO_2, Al_2O_3, and CaO, respectively) from *Webb and Courtial* [1996], which was not included in any of the regressions discussed above. In Figure 4a, a comparison is made between the measured values of sound speed (c) for this liquid and the predicted values from equation (2) and Tables 3a and 3b. The empirical model does not recover the measurements within experimental error (<1%); nor does the model of *Ghiorso and Kress* [2004], even though the Ca36.16 sample was included in their calibration of their sound speed model. In Figure 4b and 4c, a comparison is made between calculated values of isothermal compressibility (β_T) and $(\partial V/\partial P)_T$ for this liquid based directly on the measured sound speeds and the predicted values for both properties based on the fitted values in Tables 4 and 5a for use in equations (5) and (7), respectively. Although this sample was not included in any of the regressions, the experimental values for β_T and $(\partial V/\partial P)_T$ and $(\partial V/\partial P)_T$ are well recovered by the models presented in this study within the propagated experimental error (< 1.8%). This exercise indicates that the reported sound speed measurements on Ca36.16 are likely accurate (there is no reason to think otherwise), which in turn suggests that the linear, empirical model for sound speed (equation (2)) may not be optimal for calculating the compressibility of liquids in the CMAS system. Instead, the best models to use are those for β_T and $(\partial V/\partial P)_T$ given by equations (5) and (7) above, which have a theoretical foundation to their compositional dependence. They are basically equivalent, as seen by the close similarity in calculated values for K_i in Tables 4 and 5a.

Table 4. Regression Results for Equation (5) Using Data From This Study and the Literature[a]

Oxide Component	$\overline{\beta}_i$ (1673K)± 1σ (10^{-2} GPa^{-1})	$\partial\,\overline{\beta}_i / \partial T \pm$ 1σ(10^{-2} GPa^{-1} K^{-1})	K_i(1673K)(GPa)
SiO_2	7.150 ± 0.042	-	14.0
Al_2O_3	4.508 ± 0.035	-	22.2
MgO	0.615 ± 0.132	-	162.5
CaO	−1.971 ± 0.087	0.0064 ± 0.0003	−50.7

[a]Total of 153 observations; R^2 = 0.9998, and average error is 1.05%.

Table 5a. Regression Results for Equation (7) Using Data From This Study and the Literature[a]

Oxide	$\partial \overline{V}_i / \partial P$ (1673K) ± 1σ(10^{-4} cm^3 bar^{-1})	$\partial^2 \overline{V}_i / \partial P \partial T$ ± 1σ (10^{-4} cm^3 bar^{-1} K^{-1})	K_i (1673K) (GPa)	$\overline{V}_i$(1673K)(cm^3 mol^{-1})
SiO_2	−1.922 ± 0.011	-	14.0	26.86 ± 0.03
Al_2O_3	−1.692 ± 0.013	-	22.1	37.42 ± 0.09
MgO	−0.073 ± 0.016	-	160.2	11.69 ± 0.07
CaO	0.330 ± 0.015	−0.0010 ± 0.0001	−50.1	16.53 ± 0.06

[a]Total of 153 observations; R^2 = 0.9998 and average error is 1.05%. This regression excludes composition Ca36.16 (see text).

3.5. Robustness of the Models

[23] The robustness of the recommended model for $(\partial V/\partial P)_T$ (and therefore β_T) is best illustrated by performing a series of regressions on subsets of the entire experimental data set (from this study and the literature) broken out on the basis of composition: (1) CMS liquids only, (2) MAS liquids only, (3) CAS liquids only, including sample Ca36.16 (previously excluded), and (4) the entire CMAS data set. A regression of equation (7) was performed for each of the four liquid data sets and the results are presented in Tables 6a–6d. The quality of each individual regression is excellent ($R^2 \geq 0.9998$), and the fitted values for $(\partial \overline{V}_i/\partial P)_T$ for SiO_2, Al_2O_3, MgO and CaO are remarkably consistent across all four regressions; they are all within 1-sigma error of one another. (Fitted values for $(\partial \overline{V}_{MgO}/\partial P)_T$ in the regressions for CMS and MAS liquids were statistically indistinguishable from zero and therefore dropped from the regressions (Tables 6a and 6b).) Moreover, all regressions led to the same value for $(\partial^2 \overline{V}_{caO}/\partial P \partial T$, with no other component contributing to the temperature dependence of the liquid compressibility. The persistence of the small, yet positive value for $(\partial \overline{V}_{CaO}/\partial P)_T$ in all regressions (including that from *Kress and Carmichael* [1991]) strongly suggests that this feature is not an artifact of the regression, which will disappear with additional data, but instead accurately reflects how the CaO component affects the compressibility of CMAS liquids. In summary, the linear model equation of equation (7) successfully recovers the compositional and temperature dependence to $(\partial V/\partial P)_T$ for liquids in the CMAS system, which indicates that they behave as ideal solutions with respect to their compressibility at 1 bar.

4. Reevaluation of the K_0' Values for $CaMgSi_2O_6$-$CaAl_2Si_2O_8$ Liquids

[24] The new model for calculation of the isothermal compressibility of CaO-MgO-Al_2O_3-SiO_2 liquids (Table 6d) permits a reevaluation of the K_0' values for the following three liquids, $CaMgSi_2O_6$ (Di), $CaAl_2Si_2O_8$ (An), and the Di_{64}-An_{36} eutectic, for which high-pressure density data are available from shock wave measurements [*Rigden et al.*, 1988, 1989]. In the shock wave studies, both the 1-bar bulk modulus, $K_0 = 1/\beta$, and the pressure derivative, $K_0' = dK_0/dP$, were fitted to the liquid density data (for each sample) using the third-order Birch-Murnaghan EOS:

$$P = \frac{3}{2}K_0\left(R^{7/3} - R^{5/3}\right)\left[1 - \frac{3}{4}\left(4 - K_0'\right)\left(R^{7/3} - 1\right)\right] \quad (8)$$

where $R = V_0/V_0$, V_0 is the volume at zero pressure (1 bar), V_P is the volume at pressure P, K_0 is the bulk modulus at zero pressure, and K_0' is the pressure dependence of the bulk modulus at zero pressure, and assumed to be temperature-independent. In a fit for both K_0 and K_0', there is a family of paired fitted values that recovers the density data within experimental error. Therefore, values of K_0' are not uniquely constrained. Here, we use the sound speed data from this study and the density data of *Lange* [1997] to directly obtain the value of K_0 for each of three liquids: $CaMgSi_2O_6$, $CaAl_2Si_2O_8$, and Di_{64}-An_{36}. Our model recovers the experimental data for these three liquids very well (Figure 5). This permits a unique constraint to be placed on the value of K_0' for each of these three liquids on the basis of the high-pressure density data from the shock wave experiments of *Rigden et al.* [1988, 1989].

4.1. A K_0' of 6.8 for $CaMgSi_2O_6$ Liquid

[25] For $CaMgSi_2O_6$ liquid, the calculated value for $K_{T,0}(= 1/\beta_{T,0})$ from Table 6d (or Table 4) is 22.5 GPa at 1500°C, which can be compared to the shock wave experimental results of *Rigden et al.* [1989] on $CaMgSi_2O_6$ liquid, where values for both $K_{S,0}$ and K_0' (22.4 GPa and 6.9, respectively) were obtained in a fit of their high-pressure (0–38 GPa) density data to a third-order Birch-Murnaghan EOS. Their fitted value for $K_{S,0}$ (adiabatic bulk modulus) leads to a value for $K_{T,0}$ (isothermal bulk modulus) of 21.7 GPa at 1500°C, which is slightly more compressible (by 3.7%) than that obtained in this study (22.5 GPa). Additionally, the density of $CaMgSi_2O_6$ liquid at 1500°C calculated from *Lange* [1997] (2.623 g cm^{-3}) is slightly higher (by 0.5%) than that used by *Rigden et al.* [1989] (2.61 g cm^{-3}), and it makes no difference, within experimental error, to the conversion of the original shock wave U_s-U_p data to a P-V relation (P. Asimow, personal communication, 2007). If these small corrections to the

Table 5b. Regression Results From *Kress and Carmichael* [1991, Table 9][a]

Oxide Component	$\partial \overline{V}_i / \partial P$ (1673K) ± 1σ(10^{-4} cm^3 bar^{-1})	$\partial^2 \overline{V}_i / \partial P \partial T$ ± 1σ(10^{-4} cm^3 bar^{-1} K^{-1})
SiO_2	−1.89 ± 0.04	0.0013 ± 0.0003
Al_2O_3	−2.31 ± 0.11	0.0027 ± 0.0010
MgO	0.27 ± 0.14	−0.0013 ± 0.0007
CaO	0.34 ± 0.09	−0.0029 ± 0.0006

[a]Only the SiO_2, Al_2O_3, MgO and CaO components are shown for comparison to this study.

Table 6a. Regression Results for Equation (7) for CMS Liquids Only[a]

Oxide Component	$\partial \overline{V}_i / \partial P$ (1673K)± 1σ (10^{-4} cm^3 bar^{-1})	$\partial^2 \overline{V}_i / \partial P\ \partial T$ ± 1σ (10^{-4} cm^3 bar^{-1} K^{-1})
SiO_2	−1.958 ± 0.012	-
Al_2O_3	n/a	n/a
MgO	-	-
CaO	0.328 ± 0.024	−0.0011 ± 0.0001

[a]R^2 = 0.9999 and average error is 0.93% (24 observations); n/a, not applicable.

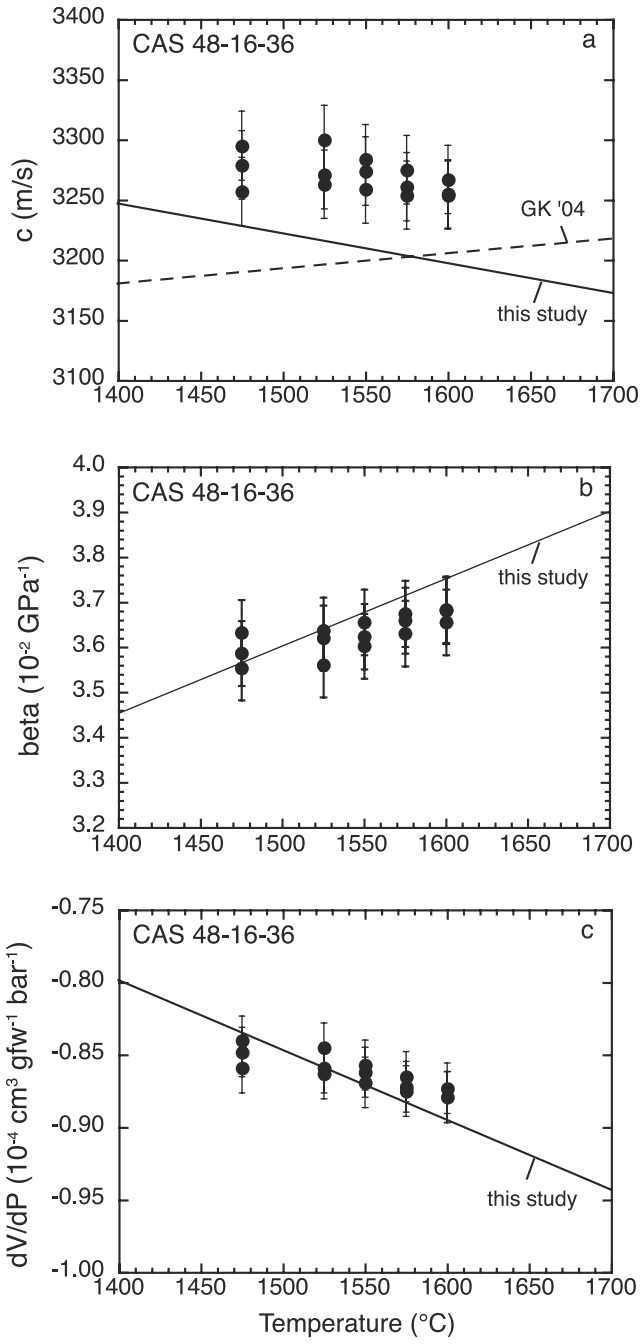

Figure 4. (a) Plot of sound speed versus temperature for a sample liquid (CAS 48-16-36) from *Webb and Courtial* [1996]. The solid line is the calculated sound speed from the model parameters in Table 3a, whereas the dashed line is the calculated sound speed from the model of *Ghiorso and Kress* [2004]. (b) Plot of β_T versus temperature for the same sample as in Figure 4a. The solid line is the calculated β_T from the model parameters in Table 4. (c) Plot of $(\partial V/\partial P)_T$ versus temperature for the same sample as in Figure 4a. The solid line is the calculated $(\partial V/\partial P)_T$ from the model parameters in Table 6d.

density and bulk modulus of $CaMgSi_2O_6$ liquid at 1500°C are made, which are based on direct measurements of density and sound speed, then only a slight change in K_0' (6.8 versus 6.9) for use in equation (8) is required to best match the high-pressure density data of *Rigden et al.* [1989] to 38 GPa within $\leq$ 0.5% (Figure 6a). This indicates excellent internal consistency in the volumetric data set for $CaMgSi_2O_6$ liquid, based on measurements made in different laboratories using different techniques.

Table 6b. Regression Results for Equation (7) for MAS Liquids Only[a]

Oxide Component	$\partial\overline{V}_i / \partial P$ (1673K) ± 1σ(10^{-4} cm^3 bar^{-1})	$\partial^2\overline{V}_i / \partial P\,\partial T$ ± 1σ(10^{-4} cm^3 bar^{-1} K^{-1})
SiO_2	−1.972 ± 0.022	-
Al_2O_3	−1.667 ± 0.105	-
MgO	-	-
CaO	n/a	n/a

[a]R^2 = 0.9999 and average error is 0.76% (19 observations); n/a, not applicable.

4.2. A K_0' of 4.7 for $CaAl_2Si_2O_8$ Liquid

[26] For $CaAl_2Si_2O_8$ liquid, the calculated value for $K_{T,0}$ (=$1/\beta_{T,0}$) from Table 6d (or Table 4) is 20.0 GPa at 1650°C, which can be compared to the shock wave experimental results of *Rigden et al.* [1989] for this liquid, where values for both $K_{S,0}$ and K_0'(17.9 GPa and 5.3, respectively) were obtained in a fit of their high-pressure (0–26 GPa) density data. Their fitted value for $K_{S,0}$ leads to a value for $K_{T,0}$ of 17.7 GPa at 1650°C, which is ~11% more compressible than that obtained in this study (20.0 GPa). Additionally, the density of $CaAl_2Si_2O_8$ liquid at 1923 K calculated from *Lange* [1997] (2.562 g cm^{-3}) is slightly higher (by 0.5%) than that used by *Rigden et al.* [1989] (2.55 g cm^{-3}), and it makes no difference, within experimental error, to the conversion of the original shock wave U_s-U_p data to a P-V relation (P. Asimow, personal communication, 2007). If these corrections to the density and bulk modulus of $CaAl_2Si_2O_8$ liquid at 1650°C are made, which are based on direct measurements, then a change in K_0'(4.7 instead of 5.3) for use in equation (8) is required to match the high-pressure density data of *Rigden et al.* [1989] to 25 GPa within $\leq$ 0.5% (Figure 6b).

4.3. A K_0' of 5.6 for the Di_{64}-An_{36} Eutectic Liquid (Model Basalt)

[27] For the Di_{64}-An_{36} eutectic liquid at 1 bar, the calculated value for $K_{T,0}$(= $1/\beta_{T,0}$) from Table 6d (or Table 4) is 22.2 GPa at 1400°C, which can be compared to the shock wave experimental results of *Rigden et al.* [1988] for this liquid, where values for both $K_{S,0}$ and K_0' (24.2 GPa and 4.85, respectively) were obtained in a fit of their high-pressure (< 25 GPa) density data. Their fitted value for $K_{S,0}$ leads to a value for $K_{T,0}$ of 23.4 GPa at 1400°C, which is ~5.4% more compressible than that obtained in this study (22.2 GPa). Additionally, the density of Di_{64}-An_{36} liquid at 1400°C calculated from *Lange* [1997]

Table 6c. Regression Results for Equation (7) for CAS Liquids Only[a]

Oxide Component	$\partial\overline{V}_i / \partial P$ (1673K) ± 1σ(10^{-4} cm^3 bar^{-1})	$\partial^2\overline{V}_i / \partial P\,\partial T$ ± 1σ (10^{-4} cm^3 bar^{-1} K^{-1})
SiO_2	−1.927 ± 0.012	-
Al_2O_3	−1.713 ± 0.019	-
MgO	n/a	n/a
CaO	0.348 ± 0.019	−0.0010 ± 0.0001

[a]R^2 = 0.9998 and average error is 1.17% (102 observations); n/a, not applicable.

Table 6d. Regression Results for Equation (7) for All CMAS Liquids[a]

Oxide Component	$\partial\overline{V}_i / \partial P$ (1673K) ± $1\sigma(10^{-4}$ cm^3 bar$^{-1})$	$\partial^2\overline{V}_i / \partial P\,\partial T$ ± $1\sigma(10^{-4}$ cm^3 bar^{-1} K$^{-1})$
SiO_2	−1.927 ± 0.010	-
Al_2O_3	−1.693 ± 0.013	-
MgO	−0.068 ± 0.015	-
CaO	0.334 ± 0.013	−0.0010 ± 0.0001

[a]R^2 = 0.9998 and average error is 1.06% (168 observations). This regression includes composition Ca36.16 (see text).

(2.618 g cm^{-3}) is slightly higher (by 0.5%) than that used by *Rigden et al.* [1988] (2.606 g cm^{-3}), and it makes no difference, within experimental error, to the conversion of the original shock wave U_s-U_p data to a P-V relation (P. Asimow, personal communication, 2007). If these corrections to the density and bulk modulus of Di_{64}-An_{36} liquid at 1400°C are made, which are based on direct measurements, then a change in K_0' (5.6 instead of 4.85) for use in equation (8) is required to best match the high-pressure density data of *Rigden et al.* [1988] to 20 GPa within $\leq$ 0.7% (Figure 6c); at 25 GPa, the deviation is 1.0%.

4.4. A Compositional Trend of K_0' Versus K_0 for $CaMgSi_2O_6$-$CaAl_2Si_2O_8$ Liquids

[28] One of the outcomes of the reexamination of K_0 and K_0' for each liquid is that they now follow a systematic trend with composition, whereas the fitted values from *Rigden et al.* [1988, 1989] do not follow a compositional pattern (Figure 7). For example, at 1900 K (1627°C), the $K_{T,0}$ value for the Di_{64}-An_{36} eutectic liquid (21.4 GPa) derived from the sound speed data is now intermediate between the $K_{T,0}$ values for $CaMgSi_2O_6$ liquid (22.1 GPa) and $CaAl_2Si_2O_8$ liquid (19.7 GPa). Perhaps more significant, the derived K_0' values also show this pattern, with the K_0' value for the Di_{64}-An_{36} eutectic liquid (5.6) intermediate between the K_0' values for $CaMgSi_2O_6$ liquid (6.8) and $CaAl_2Si_2O_8$ liquid (4.7).

5. Density of Liquid $CaMgSi_2O_6$ Versus Crystalline Diopside With Pressure

[29] With a revised estimate for the K_0' of liquid $CaMgSi_2O_6$ for use in the third-order Birch-Murnaghan EOS (equation (8)), the density of $CaMgSi_2O_6$ liquid can be calculated as a function of pressure. In Figure 8, the liquid density at 1627°C (1900 K) is compared to that for crystalline diopside between 0 and 25 GPa. The thermal expansion of crystalline diopside is reported by *Richet et al.* [1998], whereas the compressibility is obtained from the X-ray diffraction experiments of *Tribaudino et al.* [2000] from 0 to 40.8 GPa using high brilliance synchrotron radiation. The curves in Figure 8 show a density inversion between crystalline and liquid $CaMgSi_2O_6$ at ~17 GPa at 1900 K; for comparison, *Matsui* [1996] reported a density inversion at ~11 GPa at 1900 K on the basis of molecular dynamic calculations of $CaMgSi_2O_6$ melt density. The density inversion at 17 GPa occurs at a slightly higher pressure than the breakdown of diopside to Ca-perovskite ($CaSiO_3$) plus liquid at ~16 GPa [*Gasparik*, 1996]. Thus, the slope (dT/dP) of the melting curve for diopside is not predicted to

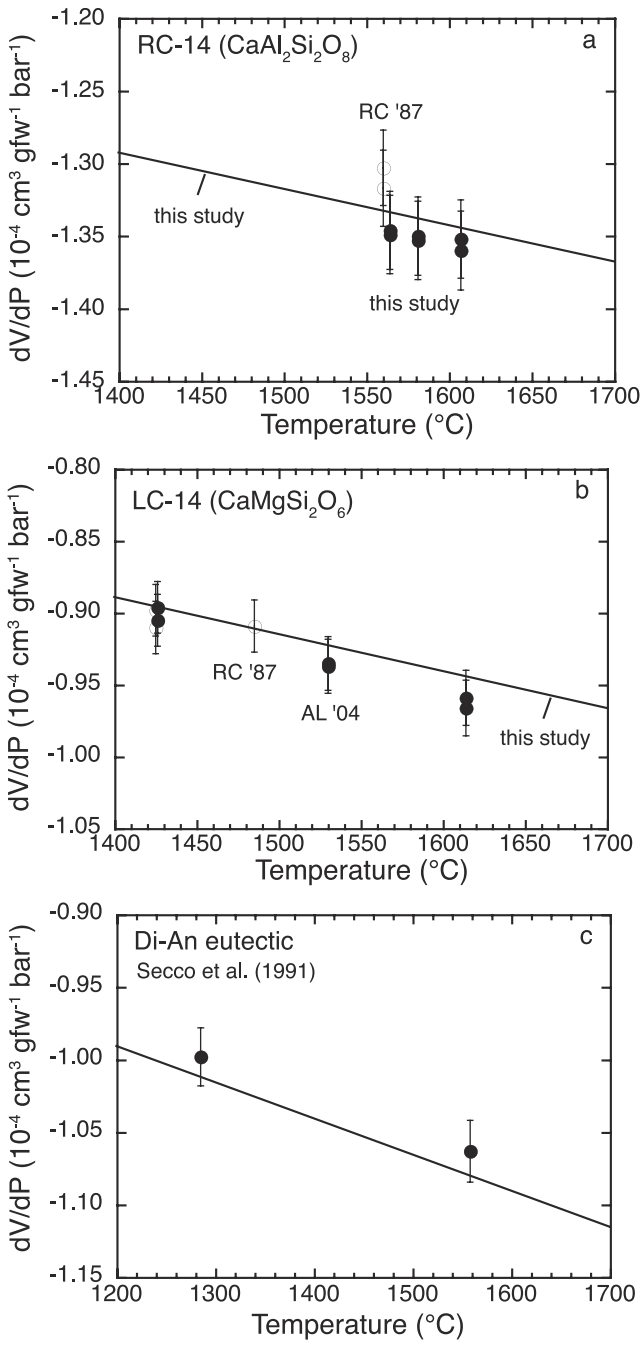

Figure 5. (a) Plot of $(\partial V/\partial P)_T$ versus temperature for $CaAl_2Si_2O_8$ liquid. Solid dots are from this study, whereas open circles are from *Rivers and Carmichael* [1987]. The solid line is the calculated $(\partial V/\partial P)_T$ from the model parameters in Table 6d. (b) Plot of $(\partial V/\partial P)_T$ versus temperature for $CaMgSi_2O_6$ liquid. Solid dots are from *Ai and Lange* [2004b], whereas open circles are from *Rivers and Carmichael* [1987]. The solid line is the calculated $(\partial V/\partial P)_T$ from the model parameters in Table 6d. (c) Plot of $(\partial V/\partial P)_T$ versus temperature for Di_{64}-An_{36} eutectic liquid (gfw is gram formula weight). Solid dots are from *Secco et al.* [1991]. The solid line is the calculated $(\partial V/\partial P)_T$ from the model parameters in Table 6d.

become negative, which is consistent with experimental observation [*Gasparik*, 1996].

5.1. Compressibility of Liquid $CaMgSi_2O_6$ Versus Crystalline Diopside With Pressure

[30] By combining the data from this study with the results from *Rigden et al.* [1989], the compressibility of $CaMgSi_2O_6$ liquid as a function of pressure can be calculated from the relation

$$\beta_T(P) = \frac{1}{K_T(P)} = -\frac{1}{V_T(P)}\left[\left(\frac{\partial P}{\partial V}\right)_T\right]^{-1} \quad (9)$$

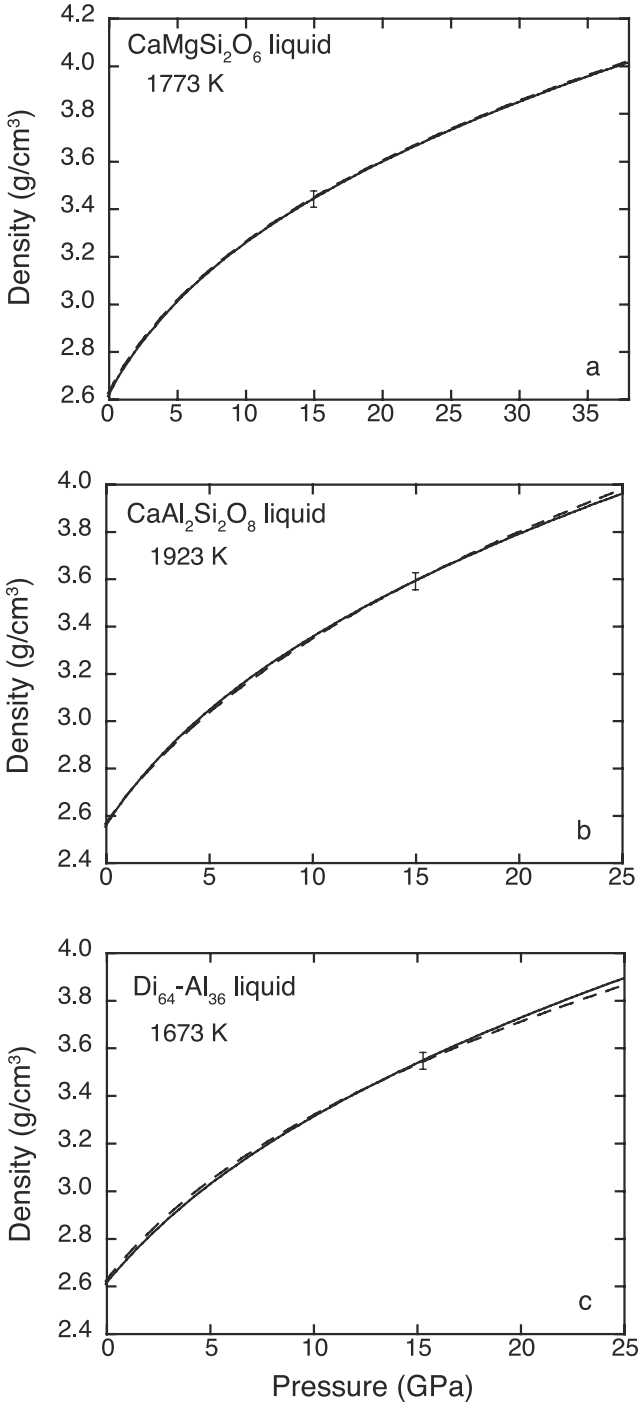

In equation (9), $(\partial P/\partial V)_T$ is the derivative of the third-order Birch-Murnaghan EOS with respect to volume [*Lange*, 2003]:

$$\left(\frac{\partial P}{\partial V}\right)_T = \frac{3}{4}\frac{K_{T,0}}{V_{T,0}}\left(R^{7/3} - R^{5/3}\right)(4 - K')R^{5/3} + \frac{3}{2}\frac{K_{T,0}}{V_{T,0}}\left(\frac{5}{3}R^{8/3} - \frac{7}{3}R^{10/3}\right) \cdot \left(1 - \frac{3}{4}(4 - K')\left(R^{2/3} - 1\right)\right) \quad (10)$$

Equation (10) allows the variation in the compressibility of $CaMgSi_2O_6$ liquid with pressure, $\beta_T(P)$, to be calculated, given $K_{T,0}$ = 22.5 GPa and K_0' = 6.8, and is shown in Figure 9 at 1627°C (1900 K). For comparison, the compressibility of crystalline diopside as a function of pressure is also shown.

[31] The two compressibility curves in Figure 9 illustrate that $CaMgSi_2O_6$ liquid is ~430% more compressible than its crystalline equivalent at 1 bar and 1900 K. The enhanced compressibility of the liquid drops sharply with increasing pressure, and is less than 50% of its 1-bar value by 5 GPa. At higher pressures, the melt compressibility decreases much more gradually. These results illustrate that there are mechanisms of compression available to liquid $CaMgSi_2O_6$ at 1 bar that are not accessible to its crystalline equivalent. Moreover, these mechanisms of compression are rapidly lost with increasing pressure between 0 and 5 GPa.

5.2. Topological Mechanisms of Compression for Liquid $CaMgSi_2O_6$ at Low Pressure

[32] The principal mechanisms of compression for minerals (also available to liquids) involve changes in either T-O-T bond angles and/or bond lengths. Minerals may also undergo an abrupt phase transition (usually first-order) to a higher-density structure with increasing pressure, which corresponds either to an abrupt change in topology (e.g., quartz to coesite) and/or cation coordination (e.g., coesite to stishovite). In contrast, liquids may undergo continuous and gradual changes in topology and/or cation coordination, which requires bonds to be broken and reformed and thus reflects the dynamic character of liquids in contrast to

Figure 6. (a) Plot of density versus pressure for $CaMgSi_2O_6$ liquid at 1773 K. The solid line is the calculated density using $K_{T,0}$ = 21.7 GPa and K_0' = 6.9 from *Rigden et al.* [1989], whereas the dashed line is the calculated density using $K_{T,0}$ = 22.5 GPa and K_0' = 6.8 from this study. (b) Plot of density versus pressure for $CaAl_2Si_2O_8$ liquid at 1923 K. The solid line is the calculated density using $K_{T,0}$ = 17.7 GPa and K_0' = 5.3 from *Rigden et al.* [1989], whereas the dashed line is the calculated density using $K_{T,0}$ = 20.0 GPa and K_0' = 4.7 from this study. (c) Plot of density versus pressure for Di_{64}-An_{36} liquid at 1673 K. The solid line is the calculated density using $K_{T,0}$ = 23.4 GPa and K_0' = 4.85 from *Rigden et al.* [1988], whereas the dashed line is the calculated density using $K_{T,0}$ = 22.2 GPa and K_0' = 5.6 from this study. All density calculations use the third-order Birch-Murnaghan EOS. The error bar in density shown at 15 GPa is 1%.

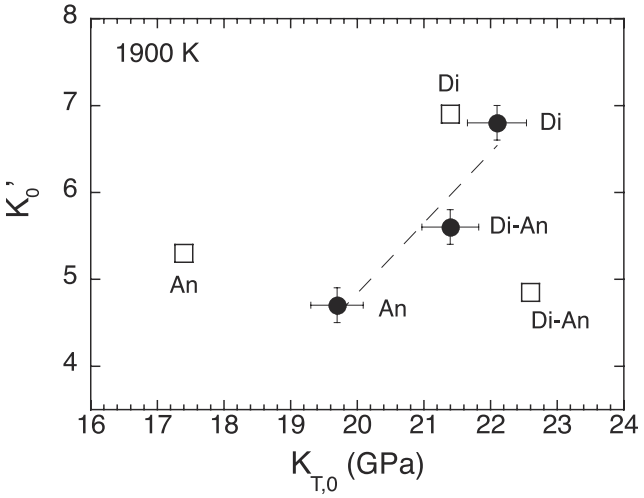

Figure 7. A plot of K_0' versus $K_{T,0}$ for three liquids at 1900 K: $CaMgSi_2O_6$ (Di), $CaAl_2Si_2O_8$ (An), and Di_{64}-An_{36} (Di-An). The open squares are from *Rigden et al.* [1988, 1989], corrected to 1900 K, whereas the solid circles are based on the new 1-bar compressibility data from this study. Estimated errors are ±2% for $K_{T,0}$ and ±0.2 for K_0'. The revised values for $K_{T,0}$ and K_0' show a systematic trend with composition.

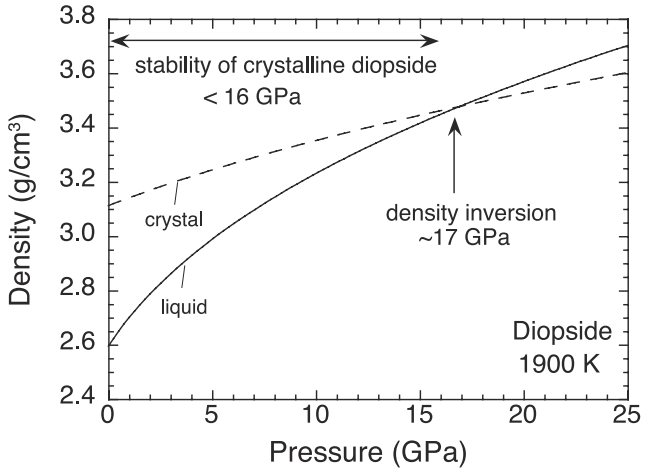

Figure 8. Plot of density versus pressure for $CaMgSi_2O_6$ liquid (solid line) at 1900 K, where $K_{T,0}$ = 22.1 GPa and K_0' = 6.8 in a third-order Birch-Murnaghan EOS (equation (8)). Also shown is the density of crystalline diopside (dashed line) at 1900 K from *Richet et al.* [1998] and *Tribaudino et al.* [2000]. The density inversion between liquid and crystal occurs at ~17 GPa at 1900 K.

solids. The continuous bond breaking that occurs in silicate liquids has been directly observed through NMR spectroscopy [e.g., *Stebbins*, 1995] and is seen in molecular dynamic simulations [e.g., *Stixrude and Karki*, 2005].

[33] The enhanced compressibility of liquid $CaMgSi_2O_6$ at low pressure (e.g., 0–5 GPa) relative to crystalline diopside (Figure 9) most likely involves topological changes in melt structure and not significant Si coordination change for two reasons. First, the compressibility of liquid $CaMgSi_2O_6$ is highest at 1 bar and then drops sharply between 0 and 5 GPa (Figure 9), indicating that modes of compression available at 1 bar are rapidly lost with increasing pressure to 5 GPa. Molecular dynamic simulations on $CaMgSi_2O_6$ liquid by *Sun et al.* [2006] indicate that the average coordination for Si^{4+} is ~4.0 at 1 bar and ~4.4 at 5 GPa. This increase in Si coordination between 0 and 5 GPa will enhance the compressibility of the liquid and not diminish it. Therefore, the precipitous drop in the melt compressibility between 0 and 5 GPa most likely involves topological changes in the melt structure that extend beyond structural changes available to crystalline diopside (i.e., changes in bond lengths and T-O-T bond angles). Second, the large volume of fusion of diopside at 1 bar and 1670 K (~16.7%) clearly indicates an average topology for liquid $CaMgSi_2O_6$ at 1 bar that is considerably different than that for crystalline diopside, and one that does not involve a change in Si coordination. Nor can the 16.7% increase in the volume of liquid $CaMgSi_2O_6$ relative to crystalline diopside be attributed simply to changes in T-O-T bond angles or bond lengths, mechanisms of thermal expansion available to crystalline diopside. In fact, with the thermal expansion equation for crystalline diopside from *Richet et al.* [1998], it takes an increase of ~2230° before the volume of crystalline diopside matches the volume of liquid diopside at its liquidus temperature (1670 K). Thus, only a substantial change in topology can adequately explain the large volume of fusion between crystalline diopside and liquid $CaMgSi_2O_6$ at 1 bar.

5.3. A Topology for $CaMgSi_2O_6$ Liquid at 1 Bar Similar to a Pyroxenoid?

[34] Insights into the topology of $CaMgSi_2O_6$ liquid at low pressure may be obtained by reviewing the 1-bar volume of fusion data not only for diopside, but also for enstatite ($Mg_2Si_2O_6$) and pseudowollastontite ($Ca_2Si_2O_6$).

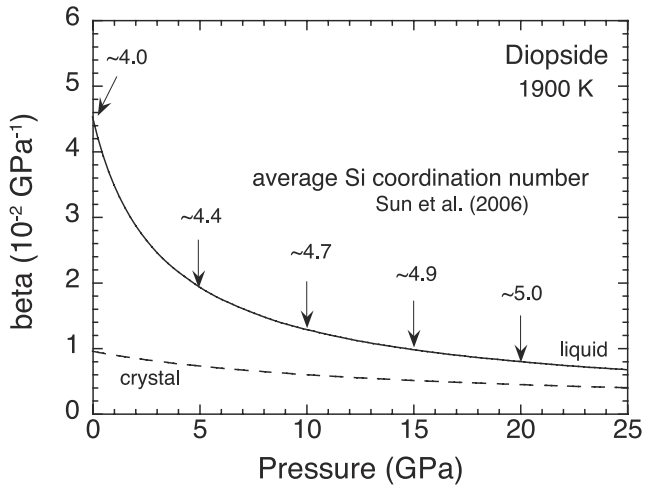

Figure 9. The isothermal compressibility of $CaMgSi_2O_6$ liquid (solid line) as a function of pressure at 1900 K calculated from equation (10) in the text, where $K_{T,0}$ = 22.1 GPa and K_0' = 6.8. Also shown is the compressibility of crystalline diopside (dashed line). The average Si coordination number in $CaMgSi_2O_6$ liquid at 5, 10, 15, and 20 GPa is from the molecular dynamic simulations of *Sun et al.* [2006].

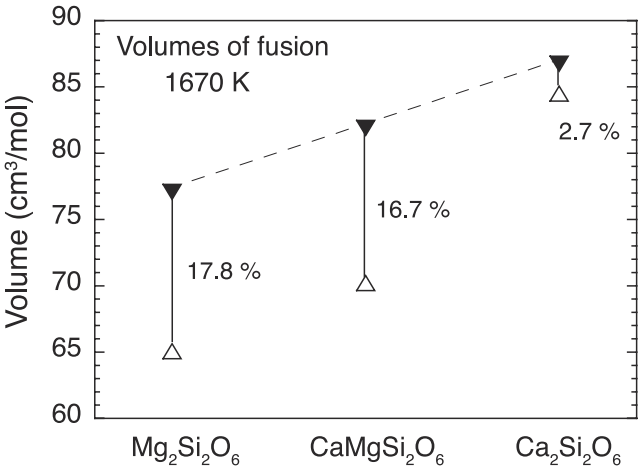

Figure 10. The molar volumes of crystalline enstatite, diopside, and pseudowollastonite at 1670 K and 1 bar (shown in open triangles and calculated from *Hugh-Jones* [1997], *Richet et al.* [1998], *Yang and Prewitt* [1999], and *Tribaudino et al.* [2000]). The molar volumes of $Mg_2Si_2O_6$, $CaMgSi_2O_6$, and $Ca_2Si_2O_6$ liquids at 1670 K and 1 bar are shown in solid triangles and are calculated from *Lange* [1997]. The small volume of fusion of pseudowollastonite is due to the large volume of the pyroxenoid relative to the pyroxenes.

In Figure 10, the molar volumes of crystalline enstatite, diopside, and pseudowollastonite (calculated from the data of *Hugh-Jones* [1997], *Richet et al.* [1998], *Yang and Prewitt* [1999], and *Tribaudino et al.* [2000]) are shown relative to the molar volumes of liquid $Mg_2Si_2O_6$, $CaMgSi_2O_6$, and $Ca_2Si_2O_6$ (calculated from *Lange* [1997]), all at 1 bar and 1670 K. The results show that the volume of fusion for pseudowollastonite (2.7%) is substantially smaller relative to those for enstatite (17.8%) and diopside (16.7%). The difference in magnitude is due entirely to the much larger crystalline volume of the pyroxenoid, pseudowollastonite, relative to those for the pyroxenes, enstatite, and diopside. The pyroxenes are made up of Si_2O_6 chains aligned along the c axis and linked through their apices to edge-shared chains of MgO_6 polyhedra and, in the case of diopside, CaO_8 polyhedra. In contrast, pseudowollastonite is a pyroxenoid in which Si_3O_9 rings alternate with layers of CaO_6 octahedra along the c axis.

[35] The small volume of fusion for pseudowollastonite suggests that $Ca_2Si_2O_6$ liquid has a topology that is not substantially different from its pyroxenoid crystalline equivalent, whereas the large volumes of fusion for enstatite and diopside suggest that their corresponding liquids ($Mg_2Si_2O_6$ and $CaMgSi_2O_6$) have topologies that are significantly different from the pyroxene crystalline equivalents. Because the volumes of the three liquids in Figure 10 vary linearly with composition, it is tempting to speculate that all three liquids have topologies that are more similar to pyroxenoids than pyroxenes. Therefore, a significant amount of the densification of $CaMgSi_2O_6$ liquid between 0 and 17 GPa (the pressure of the density inversion at 1900 K), may involve gradual, topological changes (perhaps from a 1-bar liquid structure that has more in common with pyroxenoids than with pyroxenes) in addition to a gradual increase in Si coordination.

6. Density of Liquid $CaAl_2Si_2O_8$ Versus Crystalline Anorthite

[36] As shown for liquid $CaMgSi_2O_6$ above, the density of liquid $CaAl_2Si_2O_8$ can be calculated as a function of pressure, given the sound speed results from this study and the revised K_0' estimate of 4.7 for use in the third-order Birch-Murnaghan EOS. In Figure 11, the liquid density at 1923 K is compared to that for crystalline anorthite between 0 and 25 GPa. Although anorthite is unstable above 3 GPa, its density is extraploted to higher pressure for comparison purposes. The thermal expansion of crystalline anorthite is from *Fei* [1995], whereas the compressibility is obtained from the X-ray diffraction experiments of *Angel* [2004]. The curves in Figure 11 show a density inversion between crystalline and liquid $CaAl_2Si_2O_8$ at ~1.8 GPa at 1923 K, which occurs at a higher pressure than the breakdown of anorthite to corundum and liquid at ~0.9 GPa at ~1850 K [*Goldsmith*, 1980]. Thus, the slope (dT/dP) of the anorthite fusion curve is not predicted to become negative, which is consistent with experimental observation [*Goldsmith*, 1980].

6.1. Compressibility of Liquid $CaAl_2Si_2O_8$ Versus Crystalline Anorthite With Pressure

[37] The compressibility of $CaAl_2Si_2O_8$ liquid can be calculated as a function of pressure from equation (10). For $K_{T,0}$ = 20.0 GPa and K_0' = 4.7, $\beta_T(P)$ is shown in Figure 13 from 0 to 25 GPa at 1650°C (1923 K). The extrapolated compressibility of crystalline anorthite is also shown for comparison. The two compressibility curves in Figure 12 illustrate that $CaAl_2Si_2O_8$ liquid is ~418% more compressible than its crystalline equivalent at 1 bar and 1923 K. The

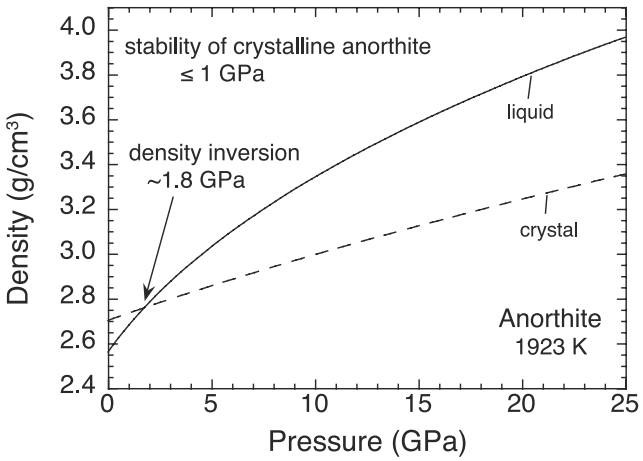

Figure 11. Plot of density versus pressure for $CaAl_2Si_2O_8$ liquid (solid line) at 1923 K, where $K_{T,0}$ = 19.7 GPa and K_0' = 4.7 in a third-order Birch-Murnaghan EOS (equation (8)). Also shown is the density of crystalline anorthite (dashed line) at 1923 K from *Fei* [1995] and *Angel* [2004]. The density inversion between liquid and crystal occurs at ~1.8 GPa at 1923 K.

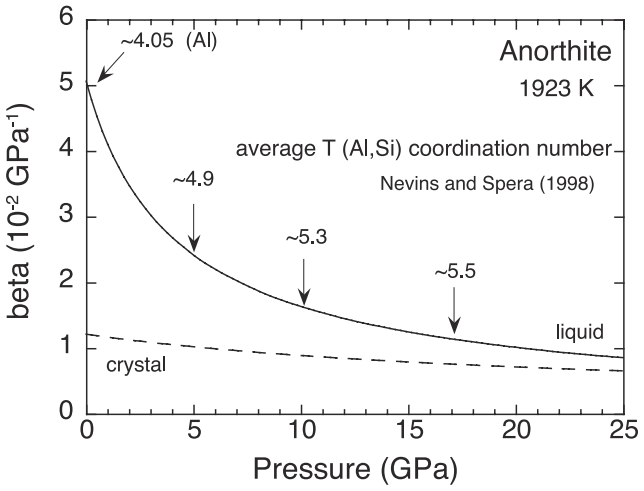

Figure 12. The isothermal compressibility of $CaAl_2Si_2O_8$ liquid (solid line) as a function of pressure at 1923 K calculated from equation (10) in the text, where $K_{T,0}$ = 19.7 GPa and K_0' = 4.7. Also shown is the compressibility of crystalline anorthite (dashed line). The average Si/Al coordination number in $CaAl_2Si_2O_8$ liquid at 5, 10, and 18 GPa is from the molecular dynamic simulations of *Nevins and Spera* [1998] at 4000 K.

enhanced compressibility of the liquid drops sharply with increasing pressure and is less than 50% of its 1-bar value by 5 GPa. At higher pressures, the melt compressibility decreases much more gradually. These results illustrate that there are mechanisms of compression available to liquid $CaAl_2Si_2O_8$ at 1 bar that are not accessible to its crystalline equivalent. Moreover, these mechanisms of compression are rapidly lost with increasing pressure between 0 and 5 GPa.

6.2. Topological Mechanisms of Compression for Liquid $CaAl_2Si_2O_6$ at Low Pressure

[38] The enhanced compressibility of liquid $CaAl_2Si_2O_8$ at low pressure (e.g., 0–5 GPa) relative to crystalline anorthite (Figure 12) most likely involves topological changes in melt structure for the same two reasons discussed for $CaMgSi_2O_6$ liquid. First, the compressibility of liquid $CaAl_2Si_2O_8$ is highest at 1 bar and then drops sharply between 0 and 5 GPa (Figure 12), indicating that modes of compression available at 1 bar are rapidly lost with increasing pressure to 5 GPa. Nuclear magnetic resonance (NMR) spectroscopic results on $CaAl_2Si_2O_8$ glass indicate up to 7% five-coordinated aluminum, $^{[5]}$Al, at 1 bar [*Neuville et al.*, 2004]. Molecular dynamic simulations on $CaAl_2Si_2O_8$ liquid at 4000 K by *Nevins and Spera* [1998] indicate an average T (Si,Al) coordination number of ~4.9 at 5 GPa. This increase in T coordination between 0 and 5 GPa will enhance the compressibility of the liquid and not diminish it. Therefore, the precipitous drop in the melt compressibility between 0 and 5 GPa, despite the increase in Al coordination, most likely involves topological changes in the melt structure. Second, the positive volume of fusion of anorthite at 1 bar (~5.3% at its melting temperature of ~1830 K) clearly cannot be attributed to the occurrence of ~7% $^{[5]}$Al and ~93% $^{[4]}$Al in the liquid compared to 100% $^{[4]}$Al in the crystal because an increase in Al coordination is expected to decrease melt volume. Nor can the 5.3% volume of fusion be attributed simply to changes in T-O-T bond angles or bond lengths, mechanisms of thermal expansion available to crystalline anorthite. In fact, with the thermal expansion equation for crystalline anorthite from *Fei* [1995], it takes an increase of ~3270° before the volume of crystalline anorthite matches the volume of liquid $CaAl_2Si_2O_8$ at its 1-bar melting temperature (~1830 K). Thus, only a substantial change in topology can adequately explain the positive volume of fusion between crystalline anorthite and liquid $CaAl_2Si_2O_8$ at 1 bar.

[39] There are several possible structural features that may make the topology of liquid $CaAl_2Si_2O_8$ different from that of crystalline anorthite, including changes in ring size distributions and the Q^n distribution. *Stebbins and Xu* [1997] documented an excess of nonbridging oxygens (NBOs) for this fully polymerized liquid, which is not found in crystalline anorthite. *Toplis et al.* [1997] proposed the occurrence of oxygen triclusters (oxygen coordinated to three TO_4 tetrahedra) to explain NBOs in tectosilicate melts, which can also be explained by the presence of some $^{[5]}$Al in the liquid [*Stebbins et al.*, 2000; *Neuville et al.*, 2004]. In terms of ring size distributions, crystalline anorthite is composed only of four-membered rings of tetrahedra, which has also been inferred for $CaAl_2Si_2O_8$ glass on the basis of X-ray diffraction results [*Taylor and Brown*, 1979]. However, a small percentage of differently sized rings in the liquid are possible, especially at high temperature. In summary, excess NBOs and the occurrence of ~7% $^{[5]}$Al are well documented features of $CaAl_2Si_2O_8$ glass, which are not found in anorthite. Further spectroscopic studies and molecular dynamic simulations are needed to identify

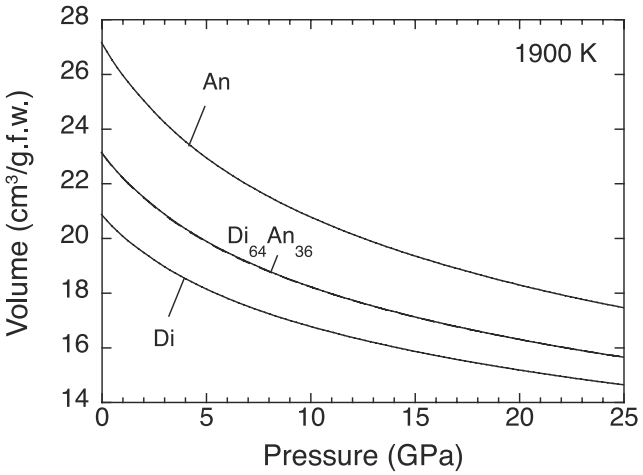

Figure 13. A plot of molar volume versus pressure for three liquids at 1900 K: $CaMgSi_2O_6$ (Di), $CaAl_2Si_2O_8$ (An), and Di_{64}-An_{36} (Di-An) calculated from equation (8) in text (solid lines). The calculated molar volume for Di_{64}-An_{36} liquid from a linear additive model of the molar volume for $CaMgSi_2O_6$ liquid (64%) and $CaAl_2Si_2O_8$ liquid (36%) (dashed line) matches that calculated from equation (8) within < 0.1%. Thus, molar volume mixes ideally for these three liquids between 0 and 25 GPa.

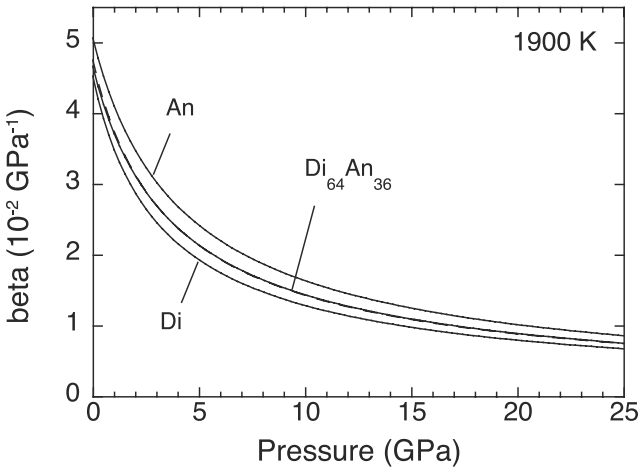

Figure 14. A plot of isothermal compressibility versus pressure for three liquids at 1900 K: $CaMgSi_2O_6$ (Di), $CaAl_2Si_2O_8$ (An), and the Di_{64}-An36 eutectic (Di-An) calculated from equation (10) in text (solid lines). The calculated isothermal compressibility for Di_{64}-An_{36} liquid from a linear additive model (in terms of volume fractions; equation (4)) of the isothermal compressibility for $CaMgSi_2O_6$ liquid (64%) and $CaAl_2Si_2O_8$ liquid (36%) (dashed line) matches that calculated from equation (10) within <2%. Thus, isothermal compressibility mixes ideally for these three liquids between 0 and 25 GPa.

additional topological differences between $CaAl_2Si_2O_8$ liquid and crystalline anorthite at 1 bar.

7. Ideal Mixing of V_T and β_T From 0 to 25 GPa for $CaMgSi_2O_6$-$CaAl_2Si_2O_8$ Liquids

[40] Given the sound speed results from this study and the revised estimates of the liquid K_0' values, the molar volumes of all three liquids, $CaMgSi_2O_6$ (Di), $CaAl_2Si_2O_8$ (An), and the Di_{64}-An_{36} eutectic, can be compared as a function of pressure (Figure 13). As originally proposed by *Rigden et al.* [1989], the molar volumes of these three liquids mix ideally up to at least 25 GPa, which is illustrated by comparing the molar volume for Di_{64}-An_{36} liquid from equation (8) (solid line in Figure 13) to that calculated additively from the molar volumes of $CaMgSi_2O_6$ liquid (64%) and $CaAl_2Si_2O_8$ liquid (36%) (dashed line in Figure 13); the deviation is $\leq$ 0.1% between 0 and 25 GPa. Linear mixing of liquid volumes along this join appears to extend to 110 GPa on the basis of recent shock wave experiments by *Asimow et al.* [2006].

[41] Similarly, the isothermal compressibility of all three liquids, $CaMgSi_2O_6$ (Di), $CaAl_2Si_2O_8$ (An), and the Di_{64}-An_{36} eutectic, can be compared as a function of pressure (Figure 14). By analogy with $CaMgSi_2O_6$ and $CaAl_2Si_2O_8$ liquids, the precipitous drop in the compressibility of Di_{64}-An_{36} liquid between 0 and 5 GPa can be attributed to the loss of topological mechanisms of compression. As observed for the molar volumes, the isothermal compressibility of $CaMgSi_2O_6$-$CaAl_2Si_2O_8$ liquids mix ideally up to at least 25 GPa, which is illustrated by comparing β_T (P) for Di_{64}-An_{36} liquid from equation (10) (solid line in Figure 13) to that calculated additively in terms of volume fractions (equation (4)) for $CaMgSi_2O_6$ liquid (64%) and $CaAl_2Si_2O_8$ liquid (36%) (dashed line in Figure 14); the deviation is <2% between 0 and 25 GPa. The clear evidence for ideal mixing of both molar volume and isothermal compressibility for $CaMgSi_2O_6$-$CaAl_2Si_2O_8$ liquids is a remarkable result given the highly variable contributions to the compressibility of $CaMgSi_2O_6$ liquid versus $CaAl_2Si_2O_8$ liquid from topological mechanisms and Al/Si coordination change between 0 and 25 GPa. It appears likely that ideal mixing of the volumetric properties of $CaMgSi_2O_6$-$CaAl_2Si_2O_8$ liquids extends to higher pressures.

[42] **Acknowledgments.** This research was supported by the National Science Foundation (EAR-0440097). Constructive comments by Paul Asimow and Carl Agee helped improve this manuscript.

References

Ai, Y., and R. Lange (2004a), An ultrasonic frequency sweep interferometer for liquids at high temperature: 1. Acoustic model, *J. Geophys. Res.*, *109*, B12203, doi:10.1029/2003JB002842.

Ai, Y., and R. Lange (2004b), An ultrasonic frequency sweep interferometer for liquids at high temperature: 2. Mechanical assembly, signal processing, and application, *J. Geophys. Res.*, *109*, B12204, doi:10.1029/2004JB003062.

Angel, R. J. (2004), Equations of state of plagioclase feldspars, *Contrib. Mineral. Petrol.*, *146*, 506–512.

Asimow, P. D., D. Sun, and T. J. Ahrens (2006), Preheated light gas gun shock experiments: Hot molybdenum and diopside-anorthite liquid Hugoniots revisited, *Eos Trans. AGU*, *87*(52), Fall Meet. Suppl., Abstract MR53D-03.

Fei, Y. (1995), *Thermal expansion, in Mineral Physics and Crystallography: A Handbook of Physical Constants, Ref. Shelf*, vol. 2, edited by T. J. Ahrens, pp. 29–44, AGU, Washington, D. C.

Gasparik, T. (1996), Melting experiments on the enstatite-diopside join to 70–224 kbar, including the melting of diopside, *Contrib. Mineral. Petrol.*, *124*, 139–153.

Ghiorso, M. S., and V. C. Kress (2004), An equation of state for silicate melts. II. Calibration of volumetric properties at 105 Pa, *Am. J. Sci.*, *504*, 679–751.

Ghiorso, M. S., M. M. Hirschmann, and P. W. Reiners (2002), The pMELTS: A revision of MELTS for improved calculation of phase relations and major element partitioning related to partial melting of the mantle to 3 GPa, *Geochem. Geophys. Geosyst.*, *3*(5), 1030, doi:10.1029/2001GC000217.

Goldsmith, J. R. (1980), The melting and breakdown reactions of anorthite at high pressures and temperatures, *Am. Mineral.*, *65*, 272–284.

Hugh-Jones, D. (1997), Thermal expansion of $MgSiO_3$ and $FeSiO_3$ ortho- and clinopyroxenes, *Am. Mineral.*, *82*, 689–696.

Katahara, K. W., C. S. Rai, M. H. Manghnani, and J. Balogh (1981), An interferometric technique for measuring velocity and attenuation in molten rocks, *J. Geophys. Res.*, *86*, 11,779–11,786.

Kress, V. C., and I. S. E. Carmichael (1991), The compressibility of silicate liquids containing Fe2O3 and the effect of composition, temperature, oxygen fugacity and pressure on their redox states, *Contrib. Mineral. Petrol.*, *108*, 82–92.

Kress, V. C., Q. Williams, and I. S. E. Carmichael (1988), Ultrasonic investigation of melts in the system Na_2O-Al_2O_3-SiO_2, *Geochim. Cosmochim. Acta*, *52*, 283–293.

Lange, R. A. (1997), A revised model for the density and thermal expansivity of K_2O-Na_2O-CaO-MgO-Al_2O_3-SiO_2 liquids between 701 and 1896 K: Extension to crustal magmatic temperatures, *Contrib. Mineral. Petrol.*, *130*, 1–11.

Lange, R. A. (2003), The fusion curve of albite revisited and the compressibility of $NaAlSi_3O_8$ liquid with pressure, *Am. Mineral.*, *88*, 109–120.

Lange, R. A., and I. S. E. Carmichael (1987), Densities of Na_2O-K_2O-CaO-MgO-FeO-Fe_2O_3-Al_2O_3-TiO_2-SiO_2 liquids: New measurements and derived partial molar properties, *Geochim. Cosmochim. Acta*, *51*, 2931–2946.

Lange, R. A., and A. Navrotsky (1992), Heat capacities of Fe_2O_3-bearing silicate liquids, *Contrib. Mineral. Petrol.*, *110*, 311–320.

Matsui, M. (1996), Molecular dynamics simulation of structures, bulk moduli, and volume thermal expansivities of silicate liquids in the system CaO-MgO-Al_2O_3-SiO_2, *Geophys. Res. Lett.*, *23*, 395–398.

Nelson, S. A., and I. S. E. Carmichael (1979), Partial molar volumes of oxide components in silicate liquids, *Contrib. Mineral. Petrol.*, *71*, 117–124.

Neuville, D. R., L. Cormier, and D. Massiot (2004), Al environment in tectosilicate and peraluminous glasses: A^{27}Al MQ-MAS NMR, *Raman, and XANES investigation, Geochim. Cosmochim. Acta*, *68*, 5071–5079.

Nevins, D., and F. J. Spera (1998), Molecular dynamics simulations of molten $CaAl_2Si_2O_8$: Dependence of structure and properties on pressure, *Am. Mineral.*, *83*, 1220–1230.

Richet, P., B. O. Mysen, and J. Ingrin (1998), High-temperature X-ray diffraction and Raman spectroscopy of diopside and pseudowollastonite, *Phys. Chem. Miner.*, *25*, 401–414.

Rigden, S. M., T. J. Ahrens, and E. M. Stolper (1988), Shock compression of molten silicate: Results for a model basaltic composition, *J. Geophys. Res.*, *93*, 367–382.

Rigden, S. M., T. J. Ahrens, and E. M. Stolper (1989), High-pressure equation of state of molten anorthite and diopside, *J. Geophys. Res.*, *94*, 9508–9522.

Rivers, M. L., and I. S. E. Carmichael (1987), Ultrasonic studies of silicate melts, *J. Geophys. Res.*, *92*, 9247–9270.

Secco, R. A., M. H. Manghnani, and T. C. Liu (1991), The bulk modulus-attenuation-viscosity systematics of diopside-anorthite melts, *Geophys. Res. Lett.*, *18*, 93–96.

Stebbins, J. F. (1995), Dynamics and structure of silicate and oxide melts: nuclear magnetic resonance studies, in *Structure, Dynamics and Properties of Silicate Melts, Rev. Mineral.*, vol. 32, edited by J. F. Stebbins, P. F. McMillan, and D. B. Dingwell, pp. 191–246, Mineral. Soc. of Am., Chantilly, Va.

Stebbins, J. F., and Z. Xu (1997), NMR evidence for excess non-bridging oxygen in an aluminosilicate glass, *Nature*, *390*, 60–62.

Stebbins, J. F., S. Kroeker, S. K. Lee, and T. J. Kiczenski (2000), Quantification of five- and six-coordinated aluminum ions in aluminosilicate and fluoride-containing glasses by high-field, high-resolution 27Al NMR, *J. Non Cryst. Solids*, *275*, 1–6.

Stixrude, L., and B. Karki (2005), Structure and freezing of $MgSiO_3$ liquid in Earth's lower mantle, *Science*, *310*, 297–299.

Sun, N., L. Stixrude, and B. B. Karki (2006), Equation of state, dynamics, electronic and atomic structure of diopside liquid at high pressure, *Eos Trans. AGU*, *87*(52), Fall Meet. Suppl., Abstract MR53C-1002.

Taylor, M., and G. E. Brown (1979), Structure of mineral glasses-I. The feldspar glasses $NaAlSi_3O_8$ $KAlSi_3O_8$, $CaAl_2Si_2O_8$, *Geochim. Cosmochim. Acta*, *43*, 61–75.

Toplis, M. J., D. B. Dingwell, K. U. Hess, and T. Lenci (1997), Peraluminous viscosity maxima in Na_2O-Al_2O_3-SiO_2 liquids: The role of triclusters in tectosilicate melts, *Geochim. Cosmochim. Acta*, *61*, 2605–2612.

Tribaudino, M., M. Prencipe, M. Bruno, and D. Levy (2000), High-pressure behavior of Ca-rich C2/c clinopyroxenes along the join diopside-enstatite ($CaMgSi_2O_6$-$Mg_2Si_2O_6$), *Phys. Chem. Miner.*, *27*, 656–664.

Webb, S., and P. Courtial (1996), Compressibility of melts in the CaO-Al_2O_3-SiO_2 system, *Geochim. Cosmochim. Acta*, *60*, 75–86.

Yang, H., and C. T. Prewitt (1999), Crystal structure and compressibility of a two-layer polytype of pseudowollastonite ($CaSiO_3$), *Am. Mineral.*, *84*, 1902–1905.

Y. Ai and R. A. Lange, Department of Geological Sciences, 1100 N. University Avenue, University of Michigan, Ann Arbor, MI 48109-1005, USA. (becky@umich.edu)